



HAL
open science

Integrated 3D geological modelling of the northern Upper Rhine Graben by joint inversion of gravimetry and magnetic data

Matthis Frey, Sebastian Weinert, Kristian Bär, Jeroen van Der Vaart, Chrystel Dezayes, Philippe Calcagno, Ingo Sass

► To cite this version:

Matthis Frey, Sebastian Weinert, Kristian Bär, Jeroen van Der Vaart, Chrystel Dezayes, et al.. Integrated 3D geological modelling of the northern Upper Rhine Graben by joint inversion of gravimetry and magnetic data. *Tectonophysics*, 2021, 813, pp.228927. 10.1016/j.tecto.2021.228927. hal-03234500

HAL Id: hal-03234500

<https://brgm.hal.science/hal-03234500v1>

Submitted on 22 Jul 2021

HAL is a multi-disciplinary open access archive for the deposit and dissemination of scientific research documents, whether they are published or not. The documents may come from teaching and research institutions in France or abroad, or from public or private research centers.

L'archive ouverte pluridisciplinaire **HAL**, est destinée au dépôt et à la diffusion de documents scientifiques de niveau recherche, publiés ou non, émanant des établissements d'enseignement et de recherche français ou étrangers, des laboratoires publics ou privés.

1 Manuscript: “Integrated 3D Geological Modelling of the Northern Upper Rhine Graben by
2 Joint Inversion of Gravimetry and Magnetic Data”

3

4 **Authors:** Matthis Frey^[a], Sebastian Weinert^[a,b], Kristian Bär^[a], Jeroen van der Vaart^[a],
5 Chrystel Dezayes^[c], Philippe Calcagno^[c], Ingo Sass^[a,b],

6 a ... Technical University of Darmstadt, Institute of Applied Geosciences,
7 Department of Geothermal Science and Technology, Schnittspahnstraße 9,
8 64287 Darmstadt, Germany

9 b ... Darmstadt Graduate School of Excellence Energy Science and
10 Engineering, Otto-Berndt-Straße 3, 64287 Darmstadt, Germany

11 c ... BRGM, 3, avenue Claude Guillemin, BP36009, 45060 Orléans cedex,
12 France

13

14 **Corresponding Author:** Matthis Frey
15 frey@geo.tu-darmstadt.de

16 Office: +49 6151 1622299

17 Mobile: +4915227522447

18 Schnittspahnstraße 9, 64287 Darmstadt, Germany

19

20 **CRedit author statement:**

21 **Matthis Frey:** Conceptualization, Investigation, Methodology, Validation, Writing - Original
22 Draft, Visualization

23 **Sebastian Weinert:** Methodology, Investigation, Writing - Review & Editing

24 **Kristian Bär:** Conceptualization, Writing - Review & Editing, Supervision, Project
25 administration, Funding acquisition

26 **Jeroen van der Vaart:** Methodology, Writing - Review & Editing, Project administration

27 **Chrystel Dezayes:** Resources, Writing - Review & Editing

28 **Phillipe Calcagno:** Resources, Writing - Review & Editing

29 **Ingo Sass:** Writing - Review & Editing, Supervision, Project administration

30 Abstract

31 The crystalline basement of the Upper Rhine Graben is a major target for deep geothermal
32 exploration due to the generally high reservoir temperatures and the increased radiogenic heat
33 production. The geothermal potential is strongly dependent on the lithology, because mainly
34 the thermal but also the hydraulic properties are affected the rock type. For this reason, the so
35 far most detailed 3D model of the basement in the northern Upper Rhine Graben was
36 developed, based on existing structural models, in particular the Hesse 3D 2.0 and GeORG
37 models. Since only a few boreholes fully penetrate the thick sediment cover, additional
38 magnetic and gravity data provided valuable information on the geometry of the deep horizons.
39 To interpret the Bouguer anomalies reasonably with respect to the crystalline basement, the
40 regional gravity field and sedimentary effect were subtracted from the observed data. In
41 comparison to the commonly applied deterministic modelling approaches, a stochastic joint
42 inversion of the gravity and magnetic anomalies was performed that utilizes the principles of a
43 Monte-Carlo-Markov-Chain simulation. For an appropriate attribution of the model units,
44 existing petrophysical databases of the region have been used and in addition, the magnetic
45 susceptibility of more than 430 rock samples was measured. High-resolution voxel models of
46 the density and susceptibility distribution were generated as a result of the inversion, which
47 allow conclusions about the crustal composition under the sedimentary formations. An
48 interpretative map of the basement geology, derived from the inversion results, is presented.

49
50

51 **Keywords:** Upper Rhine Graben, Joint Inversion, Gravity, Magnetism, 3D modelling,
52 Petrophysics

53

54 1 Introduction

55 The Upper Rhine Graben (URG), with its elevated geothermal gradient of locally more than
56 100 °C/km (Agemar et al., 2012), is one of the main targets for geothermal research and
57 exploitation in Central Europe. Besides the sedimentary horizons, the crystalline basement is
58 due to the favorable temperatures attractive for deep geothermal projects in this region (e.g.
59 Jain et al., 2015). Currently, the power plants in Landau, Insheim, Rittershoffen and Soultz-
60 sous-Forêts, use inter alia the top basement for heat or heat and power co generation. On top
61 of that, several other projects throughout the entire URG are in planning or under development.
62 The deep geothermal potential of crystalline reservoirs depends on a number of parameters,
63 which are primarily controlled by the respective lithology. First, the thermal structure of the
64 crust in the URG is, in addition to the shallow Moho depth and the deep fluid circulation patterns
65 along large-scale fault zones (Bächler et al., 2003), directly related to the radiogenic heat
66 production of the basement (Jaupart et al., 2016; Lachenbruch, 1970; Mareschal and Jaupart,
67 2013). While the highest values are measured in granites due to the increased concentration
68 of radioactive elements, the heat production of mafic rocks is on average almost one
69 magnitude smaller (Vilà et al., 2010). Likewise, the thermal conductivity of granites is by a
70 factor of 1.3 higher than in gabbros (Weinert et al., 2020a). In addition, also the hydraulic
71 conductivity of the basement is strongly influenced by the lithology. Stober and Bucher (2007)
72 could show from hydraulic test data in the Black Forest that granites have on average 2
73 magnitudes higher natural permeabilities than gneiss. This observation can be attributed, on
74 the one hand, to the significant permeability anisotropy due to layered mica minerals in
75 gneisses and, on the other hand, to the preferred fracturing along those layers with an
76 increased tendency of reclosing. In summary, felsic intrusions represent the preferred targets
77 for deep geothermal wells, whereas mafic and metamorphic rocks have less advantageous
78 thermal and hydraulic properties.

79 In the URG, knowledge about the basement structure and composition beneath the
80 sedimentary cover is limited due to the scarcity of very deep wells reaching crystalline rocks
81 and crustal-scale seismic profiles such as the DEKORP 9N line. (Brun et al., 1992; Meier and
82 Eisbacher, 1991; Meissner and Bortfeld, 1990). Key information is therefore mainly provided
83 by the crystalline outcrops at the graben borders, which for example allow the conduction of
84 analogue studies (Bär, 2012; Dezayes et al., 2021; Weinert et al., 2020a; Welsch et al., 2014).
85 Additional constraints are given by gravity and magnetic data that are available throughout the
86 whole area. In the past decades, several attempts have already been made to model the
87 crystalline basement based on the available data and to determine its properties more
88 precisely. In this context, the work of Edel and Fluck (1989), Rousset et al. (1993), Rotstein et
89 al. (2006), Edel and Schulmann (2009), Baillieux et al. (2013), Freymark et al. (2015),

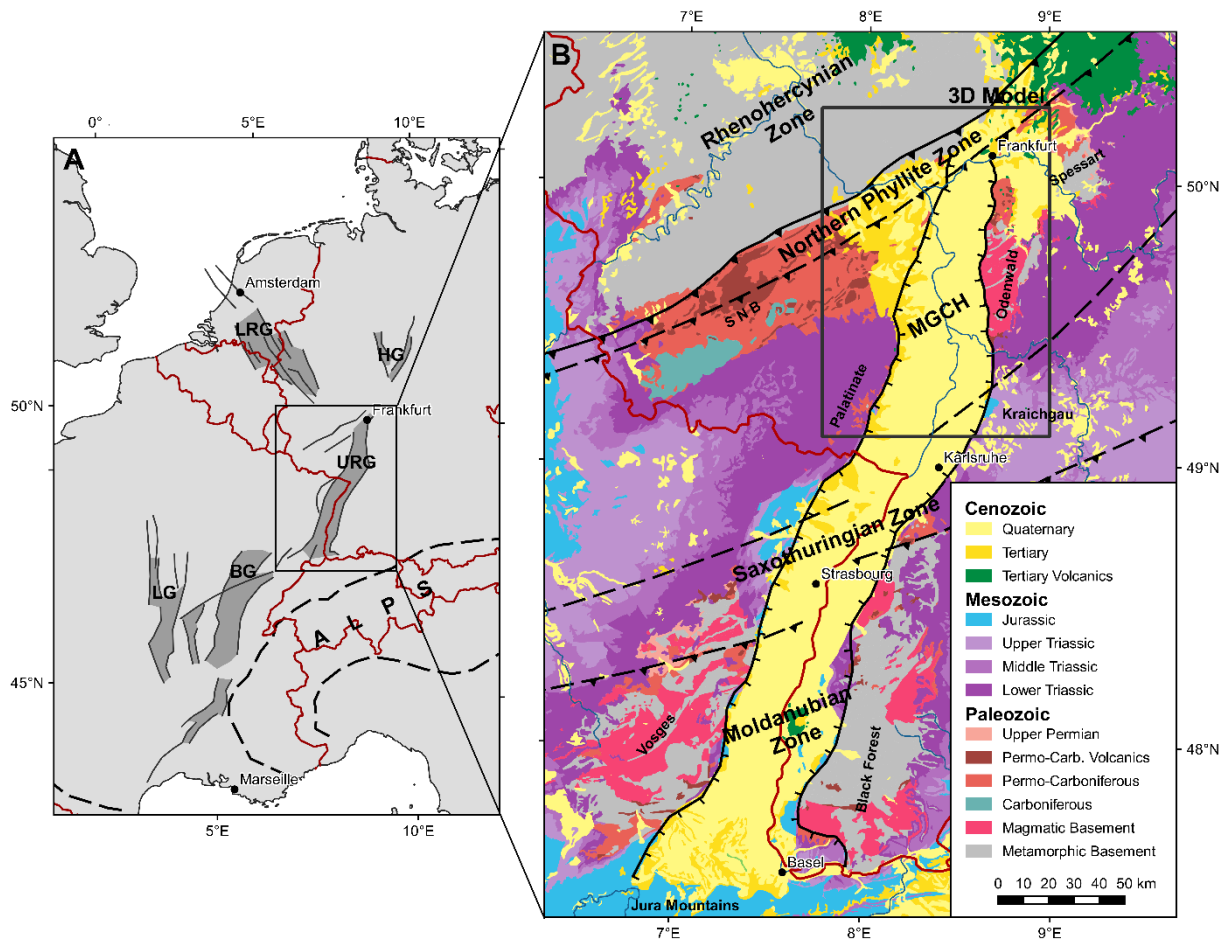
90 Freymark et al. (2017), Edel et al. (2018) and Weinert et al. (2021, in prep.) should be
91 mentioned. In contrast to these studies, a joint inversion of gravity and magnetic data was
92 performed, that has already been successfully applied in other regions (Frey and Ebbing, 2020;
93 Gallardo and Thebaud, 2012; Kamm et al., 2015). Compared to time-consuming forward
94 modelling, this approach automatically generates complex petrophysical models that are
95 moreover easily reproducible. From these, the basement lithology can be deduced, which will
96 enable more reliable estimates of geothermal potentials in the future.

97 Inversions are widely used in the geosciences to infer the distribution of petrophysical
98 properties in the subsurface from physical parameters measured at the surface, such as the
99 arrival times of seismic waves, the acceleration of gravity or the magnetic field strength (Bosch
100 and McGaughey, 2001; Li and Oldenburg, 1996, 1998). From this, information about geological
101 structures can be derived. With advancing computer capacity, calculation-intensive stochastic
102 inversions, like the Monte-Carlo-Markov-Chain method, have become increasingly important
103 in the last 2 to 3 decades (Bosch et al., 2006; Mosegaard and Tarantola, 1995). A major
104 advantage of this method compared to deterministic modelling is that a collection of possible
105 solutions is generated, allowing a statistical analysis to compute, for example, model
106 uncertainties. To obtain reliable inversion results, comprehensive information on the
107 petrophysical properties of the model units is required. Therefore, more than 430 rock samples
108 were analyzed with regard to their magnetic susceptibility. Information on the rock density was
109 taken from existing databases (Bär et al., 2020; Weinert et al., 2020b).

110 2 Geological Setting

111 2.1 Tectonics

112 The URG represents the central part of the European Cenozoic Rift System (ECRIS) (Fig. 1),
113 which consists of several tectonic grabens extending over more than 1,200 km from the
114 Mediterranean to the North Sea (Dèzes et al., 2004; Ziegler, 1992; Ziegler and Dèzes, 2005).
115 The northern URG region has a complex geological structure due to its changeful plate tectonic
116 history from the Early Paleozoic to present (Dallmeyer et al., 1995; McCann, 2008a, 2008b;
117 Ziegler, 1990). The opening of this passive continental rift started in the late Eocene as a
118 reaction to the changing lithospheric stress field in the alpine foreland (Behrmann et al., 2003;
119 Buchner, 1981; Villemin and Bergerat, 1987). Both location and orientation of the URG are
120 largely controlled by reactivation of major fault and shear zones in the basement that were
121 already established during the Variscan orogeny (Edel et al., 2007; Grimmer et al., 2017;
122 Schumacher, 2002).



123

124 Figure 1: Overview of the study area: (A) simplified map of the European Cenozoic Rift System (modified after
 125 Ziegler and Dèzes, 2005), dark grey areas represent rift-related sediment basins; (B) geological map of the URG
 126 including boundaries of the Variscan basement units. The black box shows the location of the 3D model. BG =
 127 Bresse Graben, HG = Hessian Grabens, LG = Limagne Graben, LRG = Lower Rhine Graben, MGCH = Mid-German
 128 Crystalline High, SNB = Saar-Nahe Basin, URG = Upper Rhine Graben.

129

130 The crystalline basement in the URG comprises units of the northern side of the Variscan
 131 orogenic belt that formed due to the convergence of Laurussia and Gondwana in the Middle
 132 Paleozoic (Behr et al., 1984; Franke, 2000; Giese, 1995; Kroner et al., 2008; Zeh and Gerdes,
 133 2010). The paleogeographic environment between these major continents was characterized
 134 by various micro terranes and marine basins, also known as Armorican Terrane Assemblage,
 135 which had been separated from the northern margin of Gondwana since the Cambrian
 136 (Crowley et al., 2000; Franke et al., 2017; Kemnitz et al., 2002). Accordingly, the Variscan
 137 mountain range shows strong changes in age, lithology or metamorphic grade mainly
 138 perpendicular but also parallel to the main strike direction of NE-SW (Okrusch, 1995; Oncken,
 139 1995). The subduction of the oceanic basins as a result of the advancing convergence led to
 140 the formation of extensive volcanic arcs in the Devonian and Carboniferous, exposed e.g. in
 141 the Odenwald, Black Forest and Vosges (Okrusch et al., 1995; Stein, 2001; Timmermann and
 142 Martin, 2008). The complete closure of the oceans was followed by the main collision phase

143 in Visean and Namurian times during which the individual terranes were juxtaposed and
144 pronounced continental thrusts were established along the oceanic sutures (McCann et al.,
145 2008; Oncken et al., 1999; Skrzypek et al., 2014).

146 Shortly after this collision phase, the regional stress field was reoriented towards an
147 extensional/transensional regime, resulting in a rapid collapse of the Variscides and opening
148 of numerous NE-SW striking intramontane basins, such as the Saar-Nahe Basin (Henk, 1993a,
149 1993b; Scheck-Wenderoth et al., 2008; Weber, 1995a). These were filled with erosional debris
150 from the surrounding mountain ranges, reaching a cumulative thickness of up to 10 km (Henk,
151 1992; Schäfer, 1989, 2011). In addition, the rifting was accompanied by widespread felsic to
152 mafic volcanism at the Carboniferous-Permian boundary (Seckendorff et al., 2004). In the
153 Mesozoic, sedimentation was no longer limited to these basins. The Triassic and Jurassic
154 sediments document continuous changes in the depositional environment caused by eustatic
155 sea-level fluctuations in the adjacent Arctic and Tethys Oceans (Feist-Burkhardt et al., 2008).
156 During the Upper Jurassic and Cretaceous, especially the northern URG region was affected
157 by minor volcanism (Böcker, 2015; Martha et al., 2014) and uplift movements, which led to
158 partial erosion of the sediments (Sittler, 1969, 1992). Consequently, the age of the youngest
159 preserved Mesozoic formations increases continuously from south to north, with no more
160 Mesozoic formation preserved in the northernmost part of the URG.

161 The Cenozoic formation of the URG is usually divided into two main phases (Behrmann et al.,
162 2003; Buchner, 1981; Dèzes et al., 2004; Villemin et al., 1986). During the first phase from the
163 Late Eocene to the Early Miocene, most of the crustal extension took place. In this period, the
164 main horizontal stress direction S_H was roughly NNE-SSW. In the second phase from the
165 Miocene to the present, the stress field was reoriented with S_H mainly trending in NW-SE
166 direction, leading to sinistral reactivation of faults zones parallel to the main graben axis
167 (Buchmann and Connolly, 2007; Homuth et al., 2014). While a transtensional regime in the
168 northern URG led to subsidence of the sedimentary basin, the southern part was affected by
169 transpression (Illies and Greiner, 1979; Rotstein and Schaming, 2011). Latter caused uplift in
170 the Middle and Late Miocene, resulting in erosion or non-deposition of sediments and thus in
171 a hiatus of about 10 Ma (Geyer et al., 2011; Grimmer et al., 2017). All sedimentary units as
172 well as the Variscan basement in this region are affected by intensive faulting with vertical
173 offsets between fault blocks of partly several hundred meters. The total horizontal extension
174 ranges from about 5 to 8 km and the total vertical offset reaches up to 4 km (Grimmer et al.,
175 2017; Meier and Eisbacher, 1991).

176
177 Based on analysis of gravity and magnetic data as well as field observations at the graben
178 margins, the existence of a NNE-striking crustal-scale shear zone in the crystalline basement

179 of the URG has been postulated, which may have already developed during the juxtaposition
180 of Variscan terranes in the Visean (Edel et al., 2007; Edel and Weber, 1995; Schumacher,
181 2002). According to the authors, this sinistral transform system had a considerable impact on
182 past and recent deformation in the URG due to multiple reactivations. Thus far, however, the
183 shear zone has not been detected in any boreholes, meaning that no definite statements can
184 be made about its exact location, geometry and structure.

185 2.2 Pre-Permian Crystalline Basement

186 A first definition of the Variscan basement in Central Europe was developed by Suess (1926)
187 and Kossmat (1927) and has been continuously expanded since then. The following main units
188 can be distinguished from north to south: Rhenohercynian Zone, Northern Phyllite Zone, Mid-
189 German Crystalline High (MGCH), Saxothuringian Zone and Moldanubian Zone (Figs. 1 & 2).
190 In the northern URG, the MGCH makes up the largest part of the basement. It is traditionally
191 seen as the deeply exposed northern active margin of the Armorican Terrain Assemblage, that
192 formed between the Late Devonian and Mid-Carboniferous as a result of the southward
193 subduction of the Rheic and Rhenohercynian Oceans (Hirschmann, 1995; Zeh and Gerdes,
194 2010).

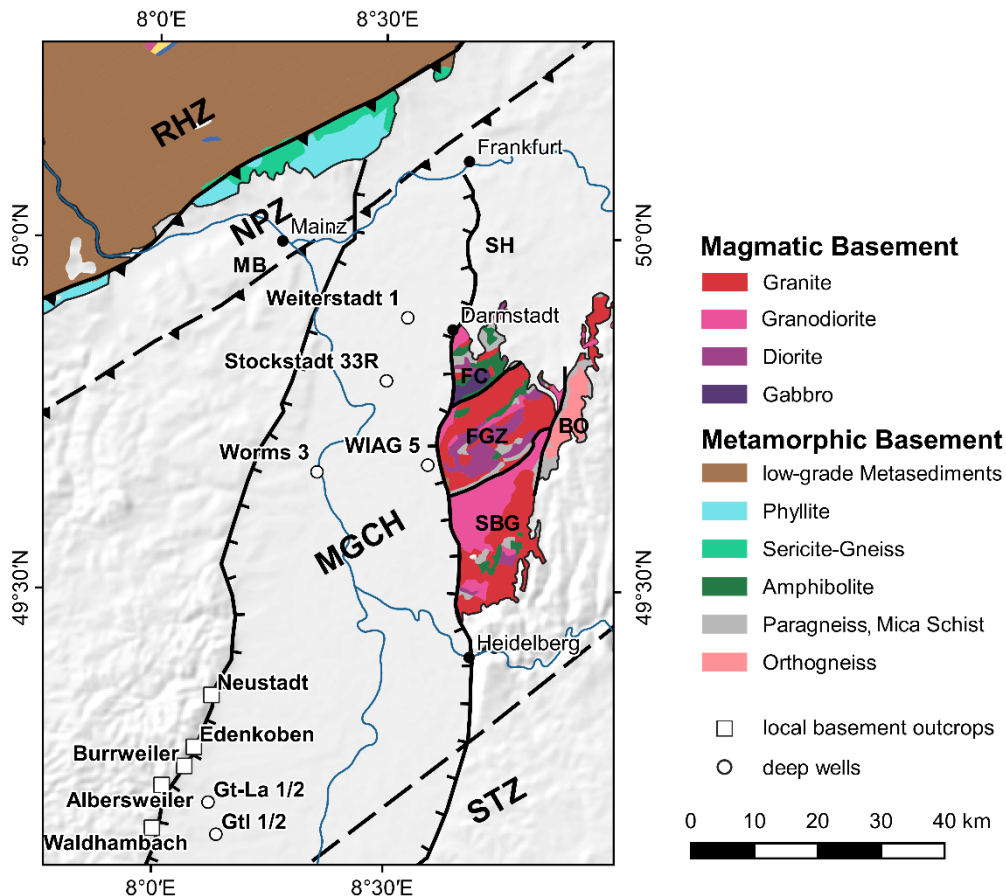
195 The largest and hence most important outcrop of the MGCH in the URG region is the crystalline
196 Odenwald (Fig. 2), which is usually divided into the eastern, metamorphic Böllstein Odenwald
197 and the western, mainly plutonic Bergsträßer Odenwald (Krohe and Willner, 1995; Stein,
198 2001). Both units are separated by the Otzberg Zone, a crustal-scale sinistral strike-slip fault.
199 The Böllstein Odenwald consists of a granitic and granodioritic orthogneiss core, surrounded
200 by metapelitic schists. According to Reischmann et al. (2001), the age of the protoliths is
201 405 ± 3 Ma, thus presumably representing relics of a Silurian/Early Devonian magmatic arc
202 (Altenberger and Besch, 1993). Due to the great lithological similarities, the Spessart is most
203 likely the northeastern extension of the Böllstein Odenwald (Weber, 1995b). The Bergsträßer
204 Odenwald consists mainly of mafic to felsic plutonic rocks, that are intruded into Early
205 Paleozoic metasediments, the so-called 'Schieferzüge' (Krohe, 1991, 1992). This unit is again
206 subdivided into the Frankenstein Complex, the Flasergranitoid Zone and the Southern Plutons,
207 each separated by large strike-slip fault zones. The first two units have a very heterogeneous
208 structure due to numerous local intrusions. The southern Bergsträßer Odenwald, in
209 comparison, is dominated by large and homogeneous plutons (Weschnitz, Tromm, Heidelberg
210 pluton). From north to south, the age of the intrusions is continuously decreasing from about
211 360 Ma in the Frankenstein Complex to about 325 Ma in the Heidelberg area (Kirsch et al.,
212 1988; Kreuzer and Harre, 1975). Likewise, the rock composition is rather mafic in the north
213 and becomes felsic towards the south (Laue et al., 1990; Okrusch et al., 1995). The

214 Bergsträßer Odenwald is hence interpreted as a transition zone from an island arc to an active
215 continental margin (Altherr et al., 1999).

216 In the Palatinate west of the URG, surface exposures of the MCGH are very limited (Flöttmann
217 and Oncken, 1992; Laue and Reischmann, 1994). The largest outcrop is in Albersweiler, where
218 orthogneisses derived from 369 ±5 Ma old magmatic protoliths are strongly intercalated with
219 metamorphosed mafic dykes (Stellrecht, 1971; Anthes and Reischmann, 1997). In the nearby
220 Waldhambach quarry, granodiorite is predominant alongside amphibolite and gneiss.
221 Metagreywackes and metapelites were found at several locations, e.g. in Burrweiler, Neustadt
222 and Weiler. Granitoid intrusions with an age of about 340 Ma are present in the Schwarzbach
223 valley, the Kaiserbach valley and Edenkoben (Frenzel, 1971). Apart from the above-mentioned
224 outcrops, only a few deep boreholes penetrate the basement in the northern URG (Bär, 2012).
225 Granitoids are predominant at most locations and additionally, amphibolites were drilled in the
226 wells Weiterstadt 1 and WIAG Hessen 5. In the well Worms 3, the basement consists of
227 fractured gneisses and cataclasites that might be related to the adjacent Worms Fault Zone
228 within the URG.

229 In the north, the MGCH borders the Northern Phyllite Zone, which is exposed in the southern
230 Taunus and Hunsrück (Anderle et al., 1995; Klügel, 1997). This zone comprises a tectonic
231 mélange of about $\frac{2}{3}$ sedimentary and $\frac{1}{3}$ volcanic rocks that were overprinted by pressure-
232 dominated greenschist-facies conditions. The boundary between the two units is a major
233 continental thrust, but the exact location is still unknown due to the complete sedimentary
234 cover. Xenoliths from the Vogelsberg can be assigned to both the Northern Phyllite Zone and
235 the MGCH, allowing to trace the tectonic contact beneath the Miocene volcanics (Martha et
236 al., 2014).

237 In the south, the MGCH transitions into the Saxothuringian Zone, which crops out in the
238 northern Black Forest and Vosges (McCann et al., 2008). This zone comprises a
239 metamorphosed, early Paleozoic shelf sequence that overlies a Neoproterozoic gneiss
240 basement. The style of the boundary between MGCH and Saxothuringia is still under debate,
241 but the location can be inferred from the gravity anomalies (Edel and Fluck, 1989; Giese,
242 1995), as the latter is characterized by a distinct high density.



243

244 Figure 2: Generalized map illustrating the basement outcrops in the northern URG region including the available
 245 wells intersecting the basement. BO= Böllstein Odenwald, FC = Frankenstein Complex, FGZ = Flaser-Granitoid
 246 Zone, MB = Mainz Basin, MGCH = Mid-German Crystalline High, NPZ = Northern Phyllite Zone, RHZ =
 247 Rhenohercynian Zone, SBG = Southern Bergsträßer Granitoids, SH = Sprendlinger Horst, STZ = Saxothuringian
 248 Zone.

249 2.3 Post-Variscan Sediments

250 The sedimentary cover and especially the Cenozoic infill of the northern URG was, in contrast
 251 to the crystalline basement, well studied by the extensive hydrocarbon exploration since the
 252 1950s (Reinhold et al., 2016; Boigk, 1981). An overview of the distribution and lithological
 253 properties of the most important horizons is given in the following.

254 The Permo-Carboniferous is overlying the crystalline basement of the northern URG on a large
 255 area. It mainly consists of erosional debris from the Variscan mountain chain and intercalated
 256 volcanics, which were deposited in several NE-SW oriented transtensional basins, like the
 257 Saar-Nahe Basin, the Hessian Basin or the Kraichgau Trough (Aretz et al., 2016; Henk, 1993b;
 258 Schäfer, 1989; Weber, 1995a). Close to the Hunsrück border fault, these deposits reach their
 259 maximum thickness of more than 6.5 km. The Saar-Nahe Basin continues to the northeast
 260 under the Cenozoic cover of the northern URG up to the Sprendlinger Horst (Molenaar et al.,

261 2015; Müller, 1996), but the thickness is much smaller here (Marell, 1989). The volcanic
262 formations consist of rhyolite, andesite and basalt, which occur in form of dikes and lava flows
263 (Hertle, 2003; Stollhofen, 1998). They are heterogeneously distributed in the URG region and
264 an accurate 3D representation is difficult due to the poor well data availability.

265 The Buntsandstein mainly consists of clastic sedimentary rocks, which reflect the terrestrial
266 conditions in the lower Triassic. This succession is dominated by uniform red-brown or light
267 gray sandstone sequences with alternating fine- and coarse-grained layers (Backhaus, 1974).
268 The Buntsandstein is exposed over a large area in the Palatinate and eastern Odenwald
269 (Backhaus, 1975; Backhaus and Heim, 1995; Backhaus and Schwarz, 2003; Dachroth, 1988).
270 In the URG, however, the horizon is only found approximately south of Worms at a depth of
271 more than 2.5 km and has a maximum thickness of about 500 m (Bär, 2012; Boigk and
272 Schöneich, 1974). Younger Triassic sediments only occur south of Heidelberg and their total
273 thickness is usually less than 500 m (Sokol et al., 2013). The Muschelkalk consists of marine
274 limestones and dolostones, documenting a full marine sedimentary environment. In contrast,
275 the Keuper, is dominated by claystones and sandstones, which are interbedded by evaporite
276 layers.

277 With the opening of the URG in the Eocene, an important sedimentary basin was again
278 established, in which marl, sandstones, carbonates, and evaporites were alternatingly
279 deposited (Doebel, 1967; Sissingh, 1998). The sedimentary conditions were predominantly
280 limnic or brackish, but at least two marine transgressions are also documented. Almost in the
281 entire northern URG, the Cenozoic graben infill has a thickness of more than 2000 m. The
282 highest thickness of 3300 m is reached close to the eastern margin between Worms and
283 Heidelberg (Doebel and Olbrecht, 1974).

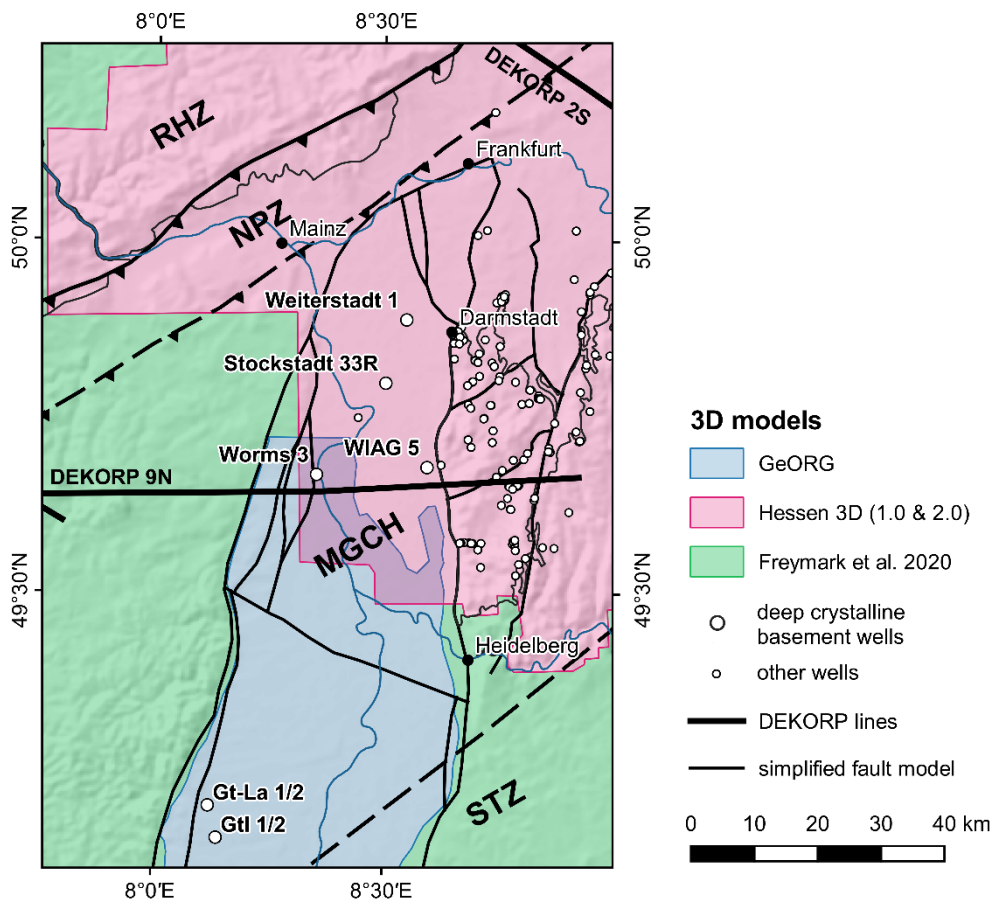
284 3 Material and Methods

285 3.1 Data

286 3.1 1 Geological Information

287 The initial 3D model of the northern URG was mainly developed by compiling existing structural
288 models (Fig. 3). In the inner part of the graben as well as in the remaining area of Hesse, the
289 detailed models of the Interreg GeORG and Hessen 3D (1.0 and 2.0) projects were used
290 (Arndt, 2012; Bär et al., 2016; Sokol et al., 2013; Weinert et al., 2021, in prep.), which are
291 based on 2D reflection seismic data, borehole data, geological profiles and isopach maps. At
292 the southern border of Hesse, where the study areas of these projects partly overlap, the depth

293 of specific horizons can deviate by several hundred meters. In order to harmonize these
 294 different results, also the recently reprocessed and reinterpreted DEKORP 9N line was
 295 incorporated (Bär et al., 2021, in prep.). Based on the GeORG and Hessen 3D models, a
 296 simplified fault model containing about a dozen of the largest faults in the northern URG region
 297 was furthermore developed. For the areas outside the URG that are not located in Hesse,
 298 information on horizon depths was extracted from the models of Freymark et al. (2015) and
 299 Freymark et al. (2020). Due to the lower density of the input data there, the model resolution
 300 is also lower but still acceptable, since the main focus was not on the graben shoulders where
 301 outcrops provide sufficient details on the crystalline basement. Additionally, the depth of the
 302 Moho and lower crust from the Freymark et al. (2020) model was used to calculate a regional
 303 gravity field (see section 3.2.1 for more details).



304
 305 Figure 3: Overview of the structural input data for the 3D modelling of the northern URG. RHZ = Renohercynian
 306 Zone, NPZ = Northern Phyllite Zone, MGCH = Mid-German Crystalline High, STZ = Saxothuringian Zone, URG =
 307 Upper Rhine Graben.

308 Apart from the mentioned modelling results, geological contacts and outcrops of large fault
 309 zones at the surface were digitized from various geological maps. To validate the initial model
 310 and the inversion result, especially with regard to the basement lithology, a database provided
 311 by the Hessian State Agency for Nature Conservation, Environment and Geology (HLNUG)

312 containing about 170 boreholes deeper than 70 m was used. However, most of the wells are
 313 located in the Odenwald or on the Sprendlinger Horst outside the URG. Therefore, information
 314 on crystalline rocks beneath the Permo-Triassic and Cenozoic graben infill is very sparse. A
 315 summary of the deep crystalline basement wells in the northern URG is given in Tab. 1.

316 Table 1: Summary the deep wells in the northern URG reaching the crystalline basement.

Well name	Depth to top basement [m]	Basement lithology	Petrophysical data available
Insheim GTI 1/2	?not published	granite	-
Landau GtLa 1/2	2487, 2550 TVD	granite	-
Stockstadt 33R	2245 MD	granodiorit	Frey et al. (2020), Weinert et al. (2020a)
Weiterstadt 1	2505 MD	granite, amphibolite	Frey et al. (2020), Weinert et al. (2020a)
WIAG Hessen 5	2180 MD	granite, amphibolites	-
Worms 3	2204 MD	fractured gneiss	Frey et al. (2020), Weinert et al. (2020a)

317

318 3.1.2 Gravity and Magnetic Data

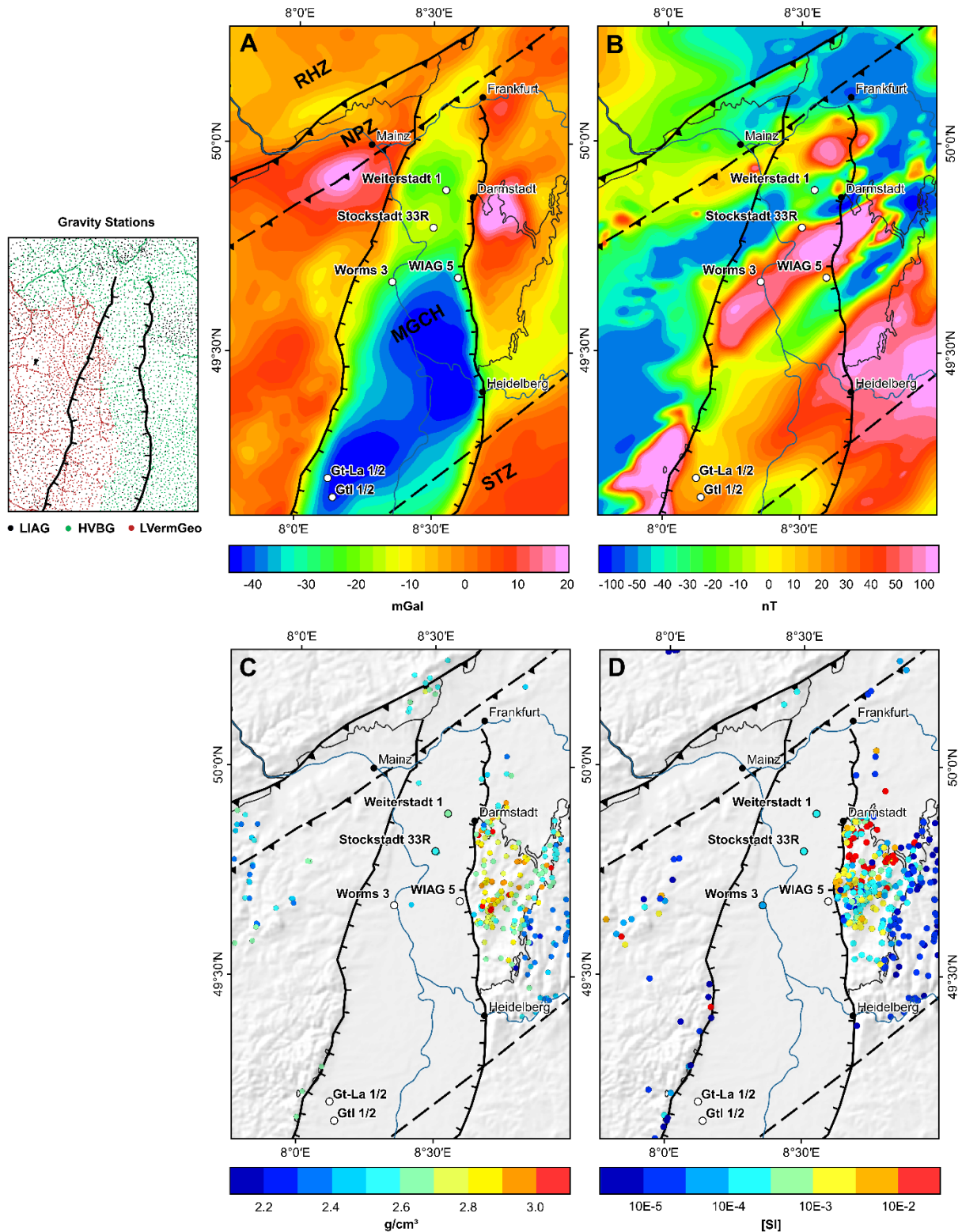
319 For the gravity modelling, a compilation of terrestrial point measurements provided by the
 320 Leibniz Institute for Applied Geophysics (LIAG), the Hessian Administration for Soil
 321 Management and Geoinformation (HVBG) and the State Agency for Surveying and Geo Base
 322 Information Rhineland-Palatinate (LVerGeo) was used. In the study area, the combined
 323 dataset consists of more than 7,000 stations with a distance between a few hundred meters
 324 and 5 km. Consequently, the resolution of the observed gravity anomalies varies considerably
 325 across the northern URG and the adjacent areas. A complete Bouguer correction has been
 326 carried out with a reference density of 2.67 g/cm³. From this point data, a Bouguer anomaly
 327 grid with a nominal resolution of 500 m was calculated by applying a minimum curvature
 328 approach (Fig. 4A).

329 The values of the gravity anomalies range from about -40 to +20 mGal. The inner part of the
 330 URG is characterized by a distinct negative anomaly that can to a large extent be explained
 331 by the relatively light sedimentary infill. The largest anomaly highs represent rather local
 332 features and are located at the mafic Frankenstein Complex and the Mainz Basin. There are
 333 moreover some broader highs, for example in the Kraichgau and the Palatinate.

334 The total magnetic field anomaly grid shown in Fig. 4B is a compiled dataset of several surface
335 and aero-geophysical surveys that have been carried out since the 1960s (Gabriel et al., 2011).
336 Airborne measurements have been performed by PRAKLA-SEISMOS between 1965 and 1971
337 with a line-spacing of 2,200 m and a point distance of approximately 65 m. Besides, the LIAG
338 and predecessor institutes conducted supplementary magnetic surveys. As for the gravity field,
339 there are therefore lateral variations of the resolution.

340 The anomalies vary from about -150 nT to more than 300 nT in the northern URG. The
341 magnetic field in the northern URG is dominated by SW-NE striking features which are most
342 likely caused by the Variscan units. Their pronunciation possibly results from the steeply
343 dipping foliation of the basement units, as observed, for example, in the Flasergranitoid Zone.
344 In addition, a laterally heterogeneous upper crust is indicated by the abundant local variations.
345 The strongest magnetic high coincides with the above-mentioned gravity anomaly at the
346 Frankenstein Complex. This anomaly extends to the SW underneath the graben infill and might
347 be furthermore associated with the magnetic high at the southeastern Palatinate. Another
348 broad positive anomaly is located in the area of the southern Odenwald plutons. Magnetic
349 anomaly lows are mostly concentrated in an SW-NE trending belt at the northern and western
350 margin of the MGCH. Another distinct negative anomaly is connected to the Flasergranitoid
351 Zone and the Böllstein Odenwald.

352 The post-Variscan deposits can generally be considered magnetically transparent due to their
353 low magnetic susceptibility (Tab. 2; Frey et al., 2020). Excluded from this assumption are the
354 Permo-Carboniferous volcanic-sedimentary horizons and the scattered tertiary volcanics
355 (Vogelsberg, Roßdorf, Otzberg, Messel). Especially in the Saar-Nahe Basin, at the Vogelsberg
356 and at the northern margin of the URG, these volcanics are source for strong and short
357 wavelength magnetic anomalies, which are also partly linked to positive gravity anomalies (e.g.
358 Mainz Basin).



359

360 Figure 4: Overview of the geophysical and petrophysical input data: (A) Bouguer anomalies in the northern URG
 361 region including map of the used gravity stations; (B) magnetic anomalies; (C) sample locations of bulk density
 362 measurements; (D) sample locations of magnetic susceptibility measurements. RHZ = Rhenohercynian Zone, NPZ
 363 = Northern Phyllite Zone, MGCH = Mid-German Crystalline High, STZ = Saxothuringian Zone, URG = Upper Rhine
 364 Graben. (Data Basis and Copyright of the gravity and magnetic data: Leibniz Institut für Angewandte Geophysik,
 365 Hannover; Hessische Verwaltung für Bodenmanagement und Geoinformation; Geobasisinformationen der
 366 Vermessungs- und Katasterverwaltung Rheinland-Pfalz).

367 3.1.3 Petrophysical Data

368 Comprehensive data on the rock density and magnetic susceptibility of the common lithologies
 369 in the northern URG were collected in order to attribute realistic petrophysical properties to the
 370 geological units in the gravity and magnetic models. Density measurements have been
 371 conducted in several previous studies and the results were compiled in the P³ database (Bär
 372 et al., 2020). A summary of the petrophysical parameters of the MGCH is additionally given in
 373 the database of Weinert et al. (2020a, b). The density distribution of the Cenozoic sediments
 374 was inferred from borehole logs of the five deep wells Eich 22, Eich 27, Eich H1, Weiterstadt
 375 1 and Worms 3 in the northern URG. Besides, measurements of the magnetic susceptibility
 376 were done with the SM-30 handheld device from GeoResults. In total about 430 samples of
 377 various geological units provided by the Institute for Rock Conservation (IfS) in Mainz were
 378 analyzed (Frey et al., 2020). Figs. 4C & 4D show the distribution of all density and susceptibility
 379 measurements in the study area. In case, very little or no information was available, e.g. in the
 380 Saxothuringian or Rhenohercynian Zones, values from the models of Freyemark et al. (2015)
 381 and Edel and Schulmann (2009) were adopted.

382 Table 2: Petrophysical properties of the main lithologies from the northern URG region that were measured on rock
 383 samples.

Rock type	Mean density [g/cm ³]	Mean Magnetic susceptibility [SI]
Granite	2.65 ± 0.028	0.0020 ± 0.0043
Granodiorite	2.72 ± 0.062	0.0017 ± 0.0020
Diorite	2.80 ± 0.052	0.0062 ± 0.0094
Gabbro	2.90 ± 0.068	0.0221 ± 0.0284
Low-grade metasediments	2.73 ± 0.088	-
Gneiss	2.65 ± 0.055	0.0012 ± 0.0041
Amphibolite	2.91 ± 0.125	0.0089 ± 0.0114
Permian and Cenozoic volcanics	2.72 ± 0.147	0.0065 ± 0.0089
Permian and Triassic sandstones	2.46 ± 0.116	1.9E-5 ± 2.2E-5
Cenozoic sandstones	2.25 ± 0.104	-

384

385 Tab. 2 summarizes petrophysical parameters for the main rock types. Because the model units
 386 (Tab. 3) are lithologically heterogeneous, a volumetric approach to calculate the model
 387 parameters was applied. This means that the parameters from Tab. 2 were weighted by the

388 area fraction of the rock type in the respective unit. For the Permo-Carboniferous, Mesozoic
389 and Cenozoic sediments, density-depth gradients were defined to account for the compaction
390 caused by the increasing load.

391 For all basement units, a parameter optimization was performed before inversion to achieve a
392 good initial fit between the forward modelled and observed potential fields. An optimization is
393 required because, apart from the Odenwald and Saar-Nahe Basin, only very few outcrops of
394 the crystalline basement are available, thus the distribution of density and magnetic
395 susceptibility is not sufficiently constrained. Moreover, samples from quarries and natural
396 outcrops are not necessarily representative for the entire model unit due to e.g. weathering
397 and exhumation effects. A summary of the initial, optimized and inverted properties is given in
398 Tab.4.

399 3.2 Methods

400 3.2.1 3D Geological Forward Modelling

401 The 3D structural modelling of the northern URG was performed with the commercial platform
402 GeoModeller (Calcagno et al., 2008; Guillen et al., 2008; Lajaunie et al., 1997), which enables
403 the development of complex geological models based on different input data and allows the
404 integration and inversion of geophysical measurements. The software uses the principles of
405 potential field interpolation and considers both structural data and stratigraphic rules to
406 construct the model (Calcagno et al., 2008; Lajaunie et al., 1997). Geological contacts are
407 considered as iso-potential surfaces and the orientation of a horizon corresponds to the
408 gradient of the field. This ensures that a consistent and smooth model is created in agreement
409 with defined geological rules, e.g. chronology and relations between the geological events.

410 The model domain has a size of 90 km in E-W direction, 130 km in N-S (see Fig. 1). It covers
411 a large part of the graben shoulders, since the main outcrops of the crystalline basement are
412 located here. The top surface of the model is the DEM given by the Shuttle Radar Topography
413 Mission (SRTM) (van Zyl, 2001) with an original resolution of one arc second and was
414 resampled to a cell size of 500 m to reduce the computational effort.

415 To separate the different sources of the gravity field, three distinct forward models, a regional,
416 a sedimentary and a basement model of the northern URG were developed that cover different
417 depth intervals of the lithosphere. A summary of all model units is given in Tab. 3. The individual
418 gravitational effects of the regional and sedimentary model were forward calculated and
419 subtracted from the observed field. This approach, also known as stripping (e.g. Hammer,
420 1963), results in a residual map of the Bouguer anomalies (Fig. 7) that provides direct insight

421 into the density distribution of the crystalline basement. Based on this product as well as the
422 magnetic anomalies and structural data, the initial basement model was created.

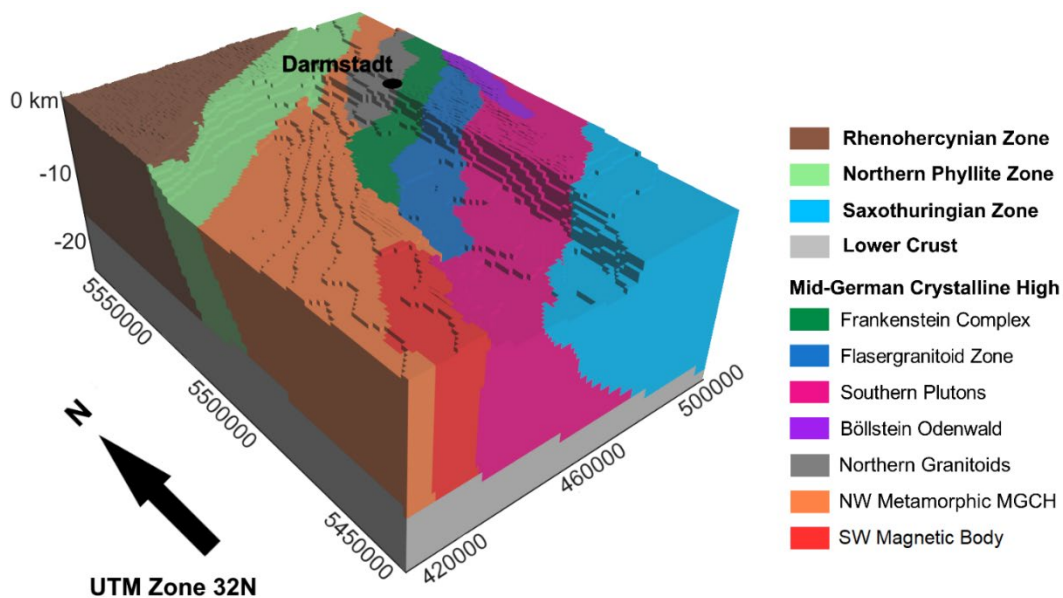
423 The basement model consists of 10 units, whereby the MGCH was divided into 7 subunits
424 (Fig. 5). According to the surface outcrops, the 4 units Frankenstein Complex, Flasergranitoid
425 Zone, Southern Odenwald and Böllstein Odenwald were defined. To explain the positive
426 gravity and magnetic anomaly in the Southeast Palatinate, an additional body with similar
427 properties as the Frankenstein Complex was introduced, referred to as the Southwestern
428 Magnetic Body in the following. The northwestern part of the MGCH was modelled as a
429 separate body, which is characterized by a high density and low susceptibility, analogously to
430 the Saxothuringian Zone. However, due to the scarcity of wells and outcrops, little information
431 is available about this zone's composition. Finally, a granitoid body of reduced density was
432 defined north of the Frankenstein Complex, which explains the local gravity low and is
433 evidenced by small outcrops and boreholes at the Sprendlinger Horst.

434 In areas where the geological contacts are not exposed, the model geometry is based on the
435 magnetic and gravity anomalies or on existing interpretations (e.g. Franke, 2000; Will et al.,
436 2015). The boundaries between the main tectonic units were modelled as southeastwards
437 dipping thrusts according to the DEKORP 2S and 9N lines (Behr and Heinrichs, 1987; Jodocy
438 and Stober, 2010; Oncken, 1998). The interfaces between the plutonic bodies of the MGCH
439 are generally assumed to be steeply dipping.

440 Table 3: Summary of the three forward models including the modelled units and their main lithology.

Model	Horizon	Main lithology	
Sedimentary Model	Cenozoic	sandstones, claystones, marl, subordinate carbonates and evaporites	
	Keuper	sandstones, claystones, subordinate evaporites	
	Muschelkalk	limestones, dolostones	
	Buntsandstein	sandstones, subordinate claystones	
	Permo-Carboniferous	sandstones, conglomerate, subordinate claystones, felsic to mafic volcanic rocks	
Regional Model	Lower Crust	mafic and metamorphic rocks	
	Lithospheric Mantle	ultramafic rocks	
Basement Model	Renohercynian Zone	low-grade metasediments	
	Northern Phyllite Zone	metasediments, metavolcanics	
	Mid-German Crystalline High	Frankenstein Complex	gabbros, amphibolites, gneiss, subordinate granitoids
		Flasergranitoid Zone	granitoids, diorites, amphibolite, gneiss
	Southern Plutons	granitoids, subordinate gneiss and amphibolites	
	Böllstein Odenwald	orthogneiss, subordinate paragneiss and granitoids	
	Northern Granitoids	granitoids	
	Southwestern Magnetic Body	very uncertain, similar to Frankenstein Complex	
	Northwestern MGCH	gneiss, metasediments	
	Saxothuringian Zone	gneiss, metasediments	

441



442

443 Figure 5: Illustration of the 3D forward model of the crystalline basement in the northern URG region.

444 3.2.2 3D Joint-Inversion

445 A structure-coupled joint inversion of gravity and magnetic data has been carried out to
446 improve the developed basement forward model and to gain detailed insights about the spatial
447 distribution of petrophysical properties. In contrast to separate inversion of the two potential
448 fields, this approach reduces the non-uniqueness of the modelling result. A stochastic inversion
449 algorithm based on a Monte-Carlo simulation is implemented in GeoModeller. The inversion
450 explores a large number of variations of the structural and petrophysical models. Those
451 realization which reduce the inconsistencies between the calculated and observed anomalies
452 are selected and allow a statistical evaluation of the inversion results. A detailed description of
453 the inversion scheme is given in Guillen et al. (2008). In the following and in Fig. 6, the specific
454 workflow applied in this study is summarized:

455 **1. A priori model**

456 The basement forward model served as the a priori information for the inversion. The
457 parametrization of the individual units is constrained by the petrophysical data and the
458 optimized densities and magnetic susceptibilities shown in Tab. 4 were used as starting
459 values. The parameters of the sediments and the lower crust were set to constant
460 reference values (density = 2.67 g/cm³ and magnetic susceptibility = 0) as their effect
461 was already considered during the forward modelling.

462 **2. Model discretization**

463 For the inversion, the continuous horizons were converted into a discrete cuboid voxel
464 model. The cell size has to be small enough to represent the geological structures
465 adequately. It should be noted, however, that the computational effort increases of
466 course with a growing number of voxels. Therefore, a uniform cell size of 1 x 1 km was
467 used in the horizontal plane. In vertical direction, a varying cell size was defined. To
468 take into account the topographic effects, a relatively small cell height of 50 m was used
469 above the mean sea level. Below, the cell height increases gradually from 500 m to
470 about 1,500 m towards the base. Consequently, the model consists in total of about
471 540,000 voxels.

472 **3. Calculation of gravity and magnetic anomalies**

473 The geophysical response of the initial density and susceptibility model is calculated
474 by summing the effect of each voxel. The calculation was done on a constant height of
475 1,000 m a.s.l. to minimize model artifacts, for example, due to the discretization.

476 **4. Disturbing the model**

477 During each iteration, either petrophysical properties or the lithology of one cell are
478 randomly changed according to the defined probability density functions. The
479 magnitude of lithology changes is controlled by the parameters shape ratio, volume
480 ratio and communality, which were set to moderate values according to the
481 documentation of GeoModeller (Intrepid Geophysics, 2017). Moreover, the top of the
482 basement and lower crust were fixed so that only the units within the upper crystalline
483 crust could be modified.

484 **5. Recalculation of the geophysical effect**

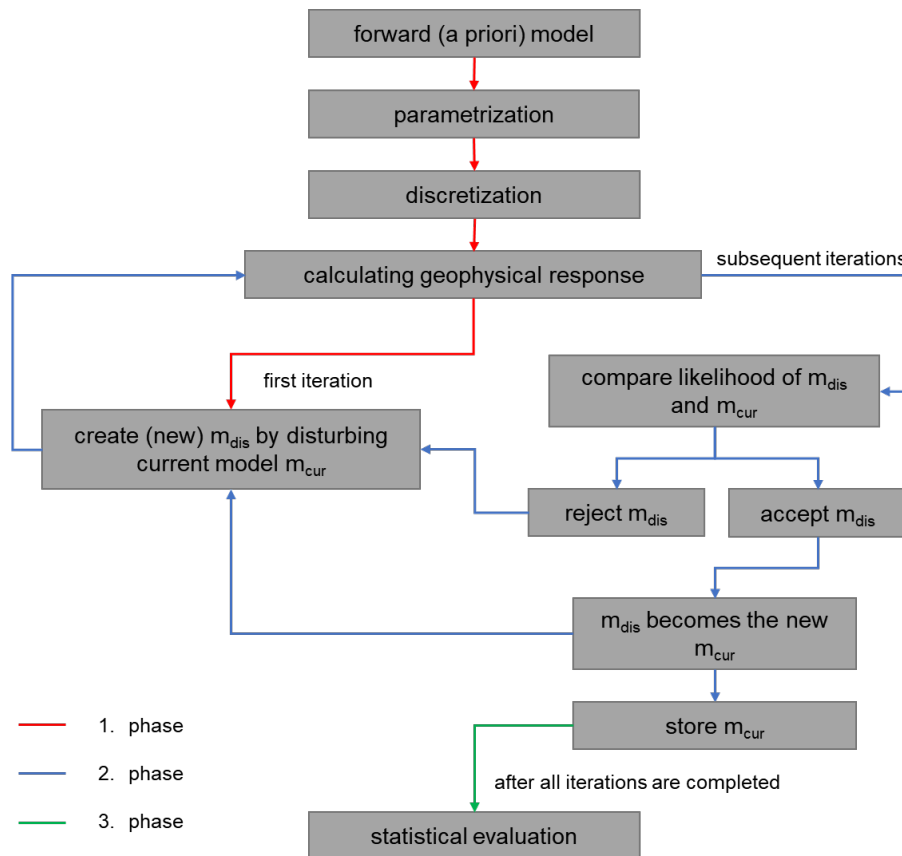
485 Based on the disturbed model, gravity and magnetic anomalies are recalculated.

486 **6. Likelihood of the disturbed model**

487 The likelihood of the disturbed model $L(m_{dis})$ is calculated as a function of the misfit with
488 the observed data and compared to the likelihood of the current model $L(m_{cur})$. If
489 $L(m_{dis}) > L(m_{cur})$, m_{dis} is accepted and becomes m_{cur} in the next iteration. If
490 $L(m_{dis}) \leq L(m_{cur})$, m_{dis} might still be accepted, depending on a randomly sampled
491 number, to ensure that the inversion does not get stuck in local minima. All accepted
492 models are stored in a separate file.

493 **7. Iteration and computing inversion result**

494 The algorithm starts over with step 4 until 500 million iterations have been calculated.
495 This high number of realizations is required to visit every cell several times. Afterwards,
496 all accepted models are combined to a summary model that contains information about
497 the mean density and susceptibility, the standard deviation, and the most probable
498 model unit of a cell.



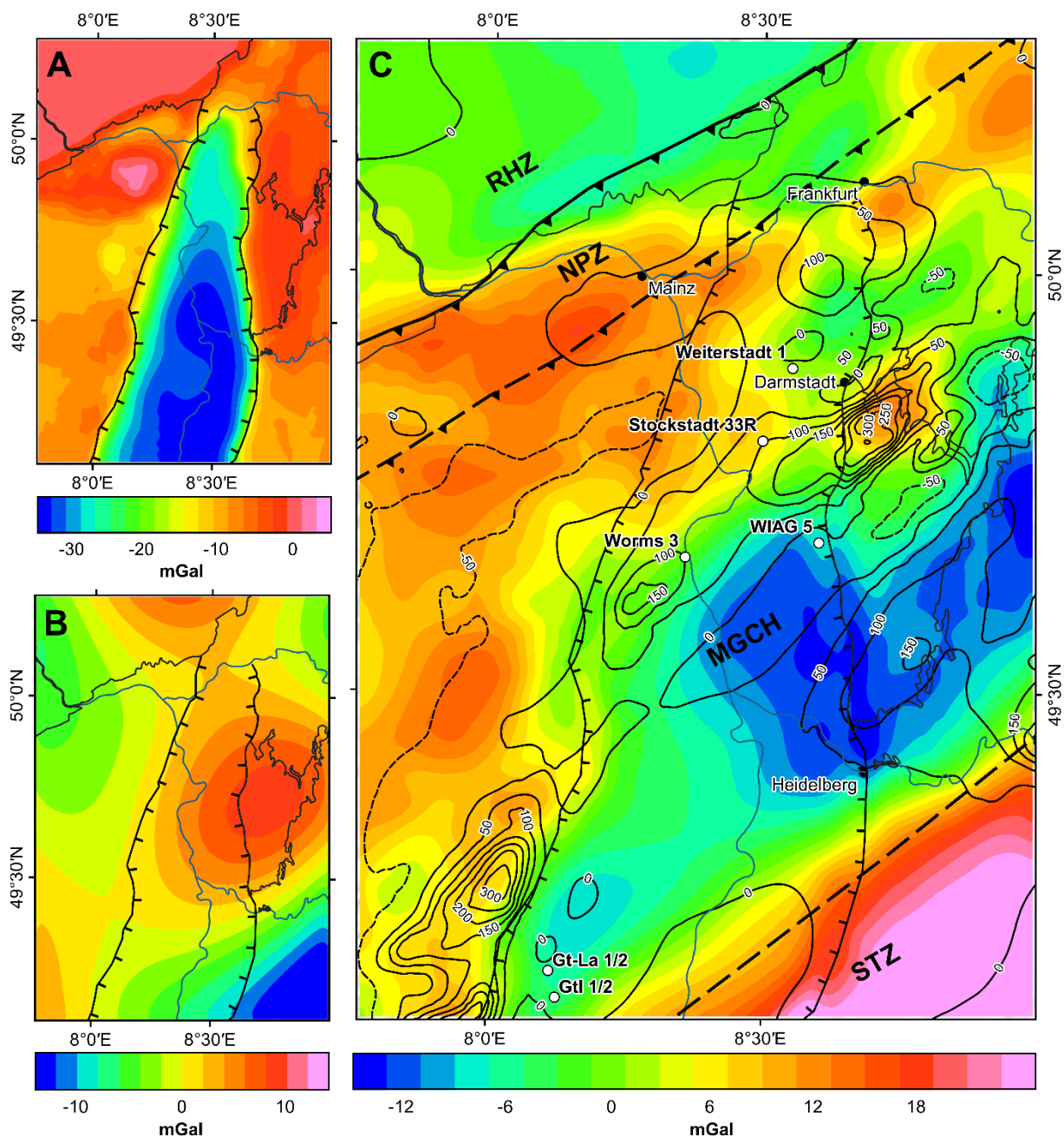
499

500 Figure 6: Generalized workflow of the stochastic joint inversion of gravity and magnetic data.

501 4 Results

502 4.1 Residual Gravity Anomalies

503 A residual Bouguer Anomaly map of the northern URG was generated by stripping the
 504 sedimentary and regional gravity effect from the observed data (Fig. 7). As a result, the field is
 505 no longer dominated by the distinct negative anomaly along the graben created by the
 506 Cenozoic infill. Instead, this product mainly represents features of the crystalline basement. As
 507 with the magnetic data, NE-SW striking features can be traced across the URG that are caused
 508 by the Variscan belt.



509

510 Figure 7: Separation of the gravity anomalies: (A) forward calculated gravitational effect of the sediments in the
 511 northern URG region; (B) forward calculated regional gravity field; (C) residual Bouguer anomalies. The isolines
 512 represent the magnetic anomalies after a reduction to the magnetic pole. RHZ = Rhenohercynian Zone, NPZ =
 513 Northern Phyllite Zone, MGCH = Mid-German Crystalline High, STZ = Saxothuringian Zone.

514 The strongest high of the residual anomalies is now located in the Saxothuringian Zone, which
 515 consists of a dense metamorphic crust and is clearly distinguishable from the granitoids of the
 516 southern MGCH. Another broad high extends over the northern/northwestern MGCH and parts
 517 of the Northern Phyllite Zone, which are covered by the thick Permo-Carboniferous deposits
 518 of the Saar-Nahe Basin. Further local anomaly highs are found at the Frankenstein Complex
 519 and at the southeastern Palatinate, both of which can be explained by the presence of mafic

520 rocks. The most pronounced gravity low is located in the granites/granodiorites area of the
521 southern Odenwald and along the SW extension of the Flasergranitoid Zone.

522 A comparison of the residual Bouguer anomalies with the pole-reduced magnetic anomalies
523 shows that there are partly strong correlations between these two potential fields, which is a
524 prerequisite for the joint inversion. This is particularly evident in the Odenwald: positive
525 correlation in the Frankenstein complex and the Böllstein Odenwald, negative correlation in
526 the southern Odenwald. A negative correlation occurs furthermore in the northwestern MGCH
527 and the Saxothuringian Zones, where gravity highs coincide with magnetic lows. In contrast, a
528 clear relationship exists not everywhere in the inner part of the URG. The separation of the
529 Flasergranitoid Zone and southern Granitoids is thus subject to larger uncertainties.

530

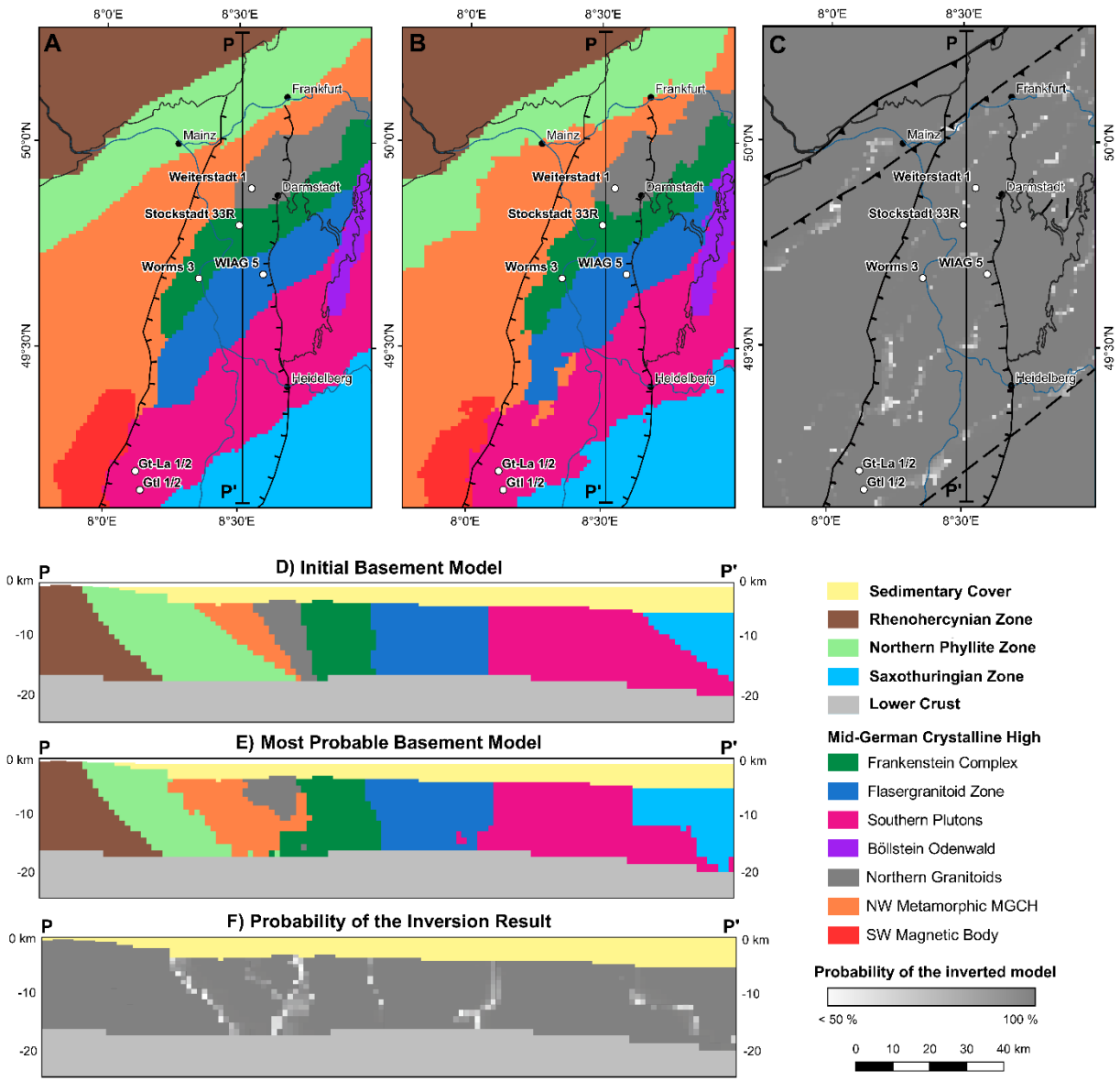
531 4.2 Inverse Model

532 Figs. 8 shows a comparison of the 3D basement forward model with the most probable model
533 of the northern URG derived from the joint inversion of gravity and magnetic data. After the
534 inversion, the interfaces are locally shifted by up to 10 km. Particularly large changes occur at
535 the boundary between MGCH and the Northern Phyllite Zone. The tectonic contact is located
536 further north and appears more irregular than presumed. Note, however, that the very similar
537 petrophysical properties of these two units (Tab. 4) make a separation with the inversion
538 approach difficult. The associated uncertainties are emphasized by the reduced probability of
539 the inversion result in this area (Figs. 8C & F). Along Profile AA' (Figs. 8D & 8E), the main
540 features of the inverted model correspond broadly to the forward model. As in the map view,
541 the reduced thickness of the Northern Phyllite Zone is apparent. The interfaces of the inverse
542 model are in general irregularly shaped, which might be related to the random character of the
543 Monte Carlo simulation. Again, the probability of inversion results reveals uncertainties of
544 locally several kilometers at the unit boundaries.

545 The mean density and susceptibility distributions at the top of the basement are illustrated in
546 Figs. 9A & 9B. Local clusters of these properties are present within and across individual model
547 units, indicating lithological variations type in the respective area. In the Odenwald, the inverted
548 density directly corresponds with the mapped lithologies: high density for mafic rocks of the
549 Frankenstein Complex, intermediate densities in the dioritic domains of the Flasergranitoid
550 Zone and relatively low densities in the predominantly felsic areas of the southern Odenwald.
551 In contrast, the susceptibility varies over more than four orders of magnitude in the study area,
552 making correlation with the lithology more difficult. Particularly high values are found along the
553 Frankenstein Complex and the Southwestern Magnetic Body, but also in the southern

554 Odenwald. Another highly magnetized body is located at the northern margin of the MGCH,
555 which is also characterized by a relatively high density, indicating the presence of intermediate
556 to mafic magmatic rocks. The metasedimentary units, in particular the Rhenohercynian, the
557 Northern Phyllite and the Saxothuringian Zone, generally exhibit very low susceptibilities. Fig.
558 9 C & 9D show the standard deviations of the inverted density and susceptibility calculated for
559 each cell of the model. Increased values occur at the model unit boundaries and in the areas
560 of high susceptibility, but are still very small relative to the mean. Consequently, a high level of
561 confidence in the inverted petrophysical models can be assumed.

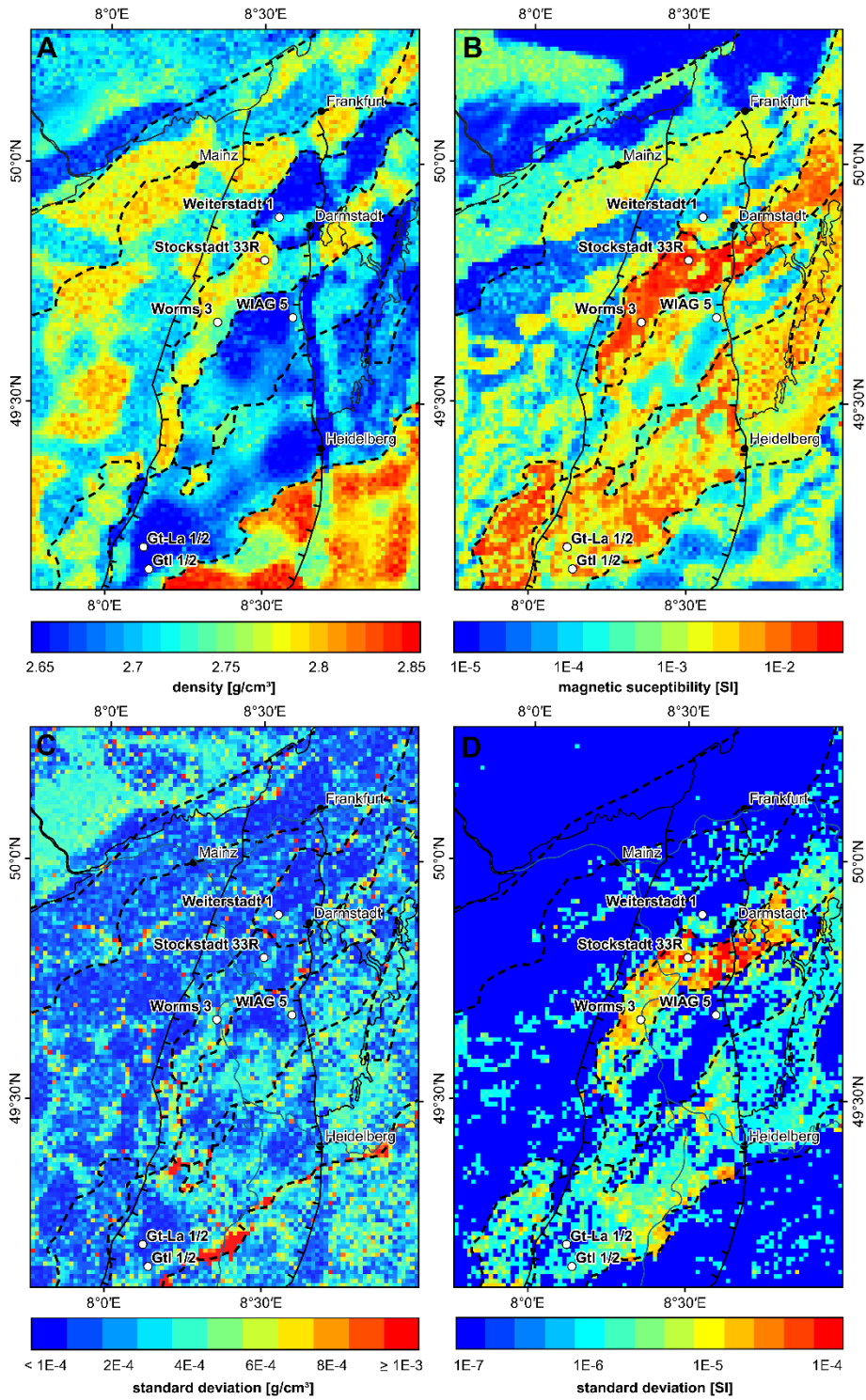
562 A comparison of the initial, optimized and inverted model parameters is given in Tab. 4 for the
563 basement units. For the rock density, only small differences can be observed between the
564 values derived from the petrophysical data and the final values. Thus, these existing databases
565 provide already a representative image of the density distribution, at least in the MGCH. By
566 contrast, the magnetic susceptibility shows significantly stronger differences between initial
567 and inverted parameters, e.g., in the Böllstein Odenwald or the Southern Plutons. These,
568 however, are still within the natural variations of the susceptibility, which were measured on
569 the outcrop samples (Tab. 2).



570

571 Figure 8: Summary of the joint inversion results: (A) forward model at the top basement; (B) most probable model
 572 after inversion at the top basement; (C) probability of the inverted model at the top basement; (D) forward model
 573 along profile PP'; (E) most probable model after inversion along profile PP'; (F) probability of the inverted model
 574 along profile PP'.

575



576

577 Figure 9: Overview of the inverted petrophysical properties: (A) mean density at the top of basement, (B) mean
 578 susceptibility; (C) & (D) standard deviation of the inverted properties for each cell. The dashed lines represent the
 579 interfaces of the inverted model units.

580

581 Table 4: Summary of petrophysical model parameters. Magnetic properties were only considered in the basement
582 model. The properties of the basement units were derived from the available petrophysical databases (initial values)
583 and then optimized (optimized values; see Section 3.1.3 for more details). During the joint inversion, the anomaly
584 misfit is further reduced by adjusting the property distribution.

585

Model	Horizon	Initial density [g/cm ³]	Opt. density [g/cm ³]	Inverted density [g/cm ³]	Initial mag. susc. [SI]	Opt. mag. susc. [SI]	Inverted mag. susc. [SI]
Sedimentary Model	Cenozoic	2.0 – 2.63	-	-	-	-	-
	Keuper	2.45 – 2.65	-	-	-	-	-
	Muschelkalk	2.70	-	-	-	-	-
	Buntsandstein	2.40 – 2.65	-	-	-	-	-
	Permo-Carboniferous	2.48 – 2.65	-	-	-	-	-
Regional Model	Lower Crust	2900	-	-	-	-	-
	Lithospheric Mantle	3300	-	-	-	-	-
Basement Model	Renohercynian Zone	2.715	2.71	2.706 ± 0.027	0.0001	0.0001	0.0003 ± 0.0004
	Northern Phyllite Zone	2.74	2.74	2.742 ± 0.030	0.0001	0.0001	0.0003 ± 0.0006
	Frankenstein Complex	2.80	2.76	2.752 ± 0.026	0.0082	0.01	0.0167 ± 0.0242
	Flasergranitoid Zone	2.71	2.68	2.685 ± 0.022	0.0032	0.001	0.0022 ± 0.0030
	Southern Plutons	2.695	2.69	2.687 ± 0.019	0.0022	0.004	0.0107 ± 0.0127
	Böllstein Odenwald	2.66	2.68	2.676 ± 0.017	0.0014	0.003	0.0071 ± 0.0081
	Northern Granitoids	2.685	2.685	2.672 ± 0.023	0.001	0.0007	0.0012 ± 0.0025
	Southwestern Magnetic Body	2.74	2.73	2.736 ± 0.022	0.01	0.01	0.0130 ± 0.0166
	Northwestern MGCH	2.735	2.75	2.747 ± 0.030	0.001	0.0005	0.0013 ± 0.0019
	Saxothuringian Zone	2.80	2.795	2.798 ± 0.021	0.001	0.0003	0.0011 ± 0.0013

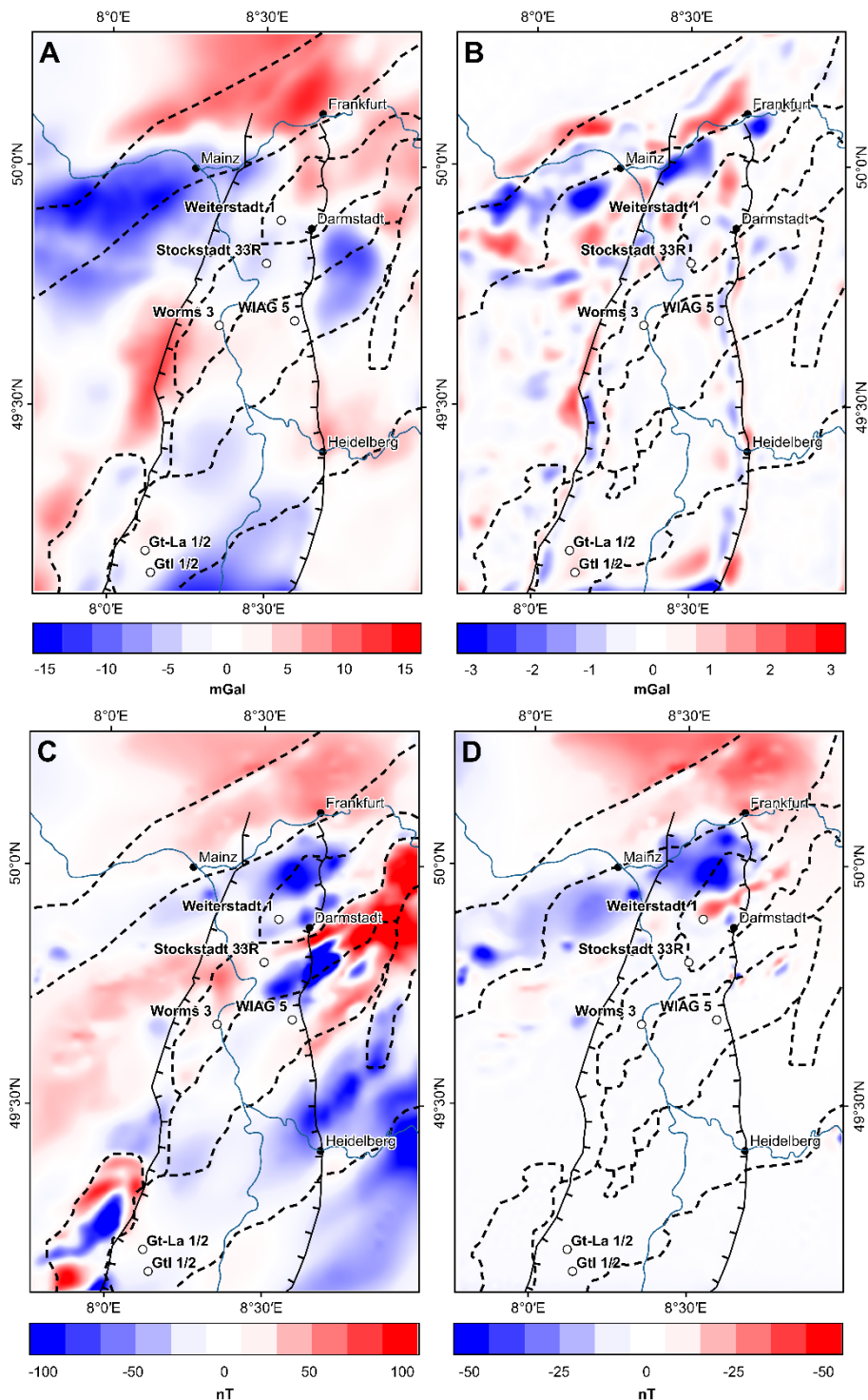
586

587

588

589

590 4.3 Model Misfit



591

592 Fig. 10: Misfit between modelled and observed anomalies: (A) misfit of the forward modelled residual Bouguer
 593 anomalies; (B) misfit of the inverted residual Bouguer anomalies; (C) misfit of the forward calculated magnetic
 594 anomalies; (D) misfit of the inverted magnetic anomalies. The dashed lines represent the interfaces of the initial (A
 595 & C) respectively inverted model units (B & D).

596 Fig. 10 shows the misfits between the observed and forward modelled respectively inverted
 597 potential fields. The forward model is able to describe the main features of the Bouguer

598 anomalies and parts of the magnetic anomalies, but the RMS misfit is still relatively high with
599 5.3 mGal and 42.1 nT. Particularly large differences can be observed at the transition from the
600 MGCH to the Northern Phyllite Zone. Moreover, the magnitude of the magnetic anomalies is
601 usually underestimated. After the inversion, the RMS misfit is with 0.6 mGal and 11.0 nT
602 reduced by 90 % and 75 %, respectively. The largest deviations of the Bouguer anomalies are
603 still found in the northwestern MGCH and the Northern Phyllite Zone as well as along the main
604 border faults, but the differences between the observation and the model are now relatively
605 small (± 4 mGal). In addition, the modelled magnetic anomalies are significantly improved,
606 especially in the inner part of the URG. Larger differences still exist in the north, possibly due
607 to the influence of the volcanic rocks of the Vogelsberg and Permo-Carboniferous, which were
608 not considered during inversion.

609 5 Discussion

610 5.1 Uncertainties of Applied Methods

611 A detailed 3D basement model of the northern URG was developed by integrating available
612 structural information as well as gravity and magnetic data. Especially the stripping of the
613 sedimentary and regional gravity field (Fig. 7) was helpful as the residual Bouguer anomalies
614 provide key insights on the composition of the crystalline upper crust. However, it should be
615 noted that this approach is affected by various uncertainties. First of all, the horizon depths in
616 the sediment model are subject to errors that have an impact on the calculated gravity field of
617 several mGal. Likewise, the defined density distribution at depth is uncertain since it is only
618 supported by a few data points. A laterally homogeneous density gradient was assumed, which
619 may not reflect the actual variations within the sediments. Particularly large uncertainties exist
620 in connection with the Permo-Carboniferous volcanic formations. They are typically
621 characterized by a variable thickness and composition, with the density ranging from 2.6 to
622 more than 3.0 g/cm³, thus causing the gravity effect to vary considerably. In the Mainz Basin,
623 these volcanic horizons have a significant but hardly quantifiable impact on the gravity
624 anomalies, which makes the separation of the underlying MGCH and the Northern Phyllite
625 Zone challenging.

626 For the modelling of the magnetic anomalies, the susceptibility of all post-Variscan deposits
627 was set to 0 [SI]. This assumption is roughly valid for the clastic and carbonate sediments, but
628 Permo-Carboniferous and Cenozoic volcanic deposits show in general higher susceptibilities.
629 They might be sources of stronger magnetic anomalies in the Saar-Nahe Basin, on the
630 Spredlinger Horst and in the northernmost URG. Ignoring their effect leads most likely to the
631 increased anomaly misfits in these areas (Fig. 10) and can partly corrupt the inversion result.

632 An improved sediment model including the volcanic intercalations and better knowledge about
633 the petrophysical properties would consequently result in a more accurate calculation of the
634 gravity and magnetic anomalies. This, however, would require an extension of the
635 petrophysical database and an in-depth analysis of the existing well logs.

636 Moreover, also the regional gravity model is affected by some uncertainty. On the one hand,
637 the seismic profiles and receiver function data on which the depth of the lower crust and the
638 Moho are based are very sparse. On the other hand, this data can be subject to errors of
639 several kilometers. This can easily lead to variations in the calculated gravity effect of up to 10
640 mGal. But these uncertainties influence the inversion only to a limited extent because the
641 wavelength is generally very long.

642 The basement model resulting from the joint inversion is able to describe the gravity and
643 magnetic anomalies very well (Figs. 10B & 10D). It can therefore be assumed, that the final
644 density and susceptibility distributions are realistic representations of the crystalline basement.
645 Nevertheless, due to the random character of the Monte Carlo simulation also geologically
646 implausible features might be generated, making a thorough plausibility check of the inversion
647 result necessary. Furthermore, the inversion result depends to a large extent on the inversion
648 parameters and the starting model, but the general agreement with the crystalline outcrops at
649 the graben shoulders and the wells in the northern URG shows that the selected initial
650 conditions are reasonable. Indications of model uncertainties are provided by the probabilities
651 of the inverted 3D structures (Figs. 8C & 8F).

652 5.2 Basement Structure and Composition

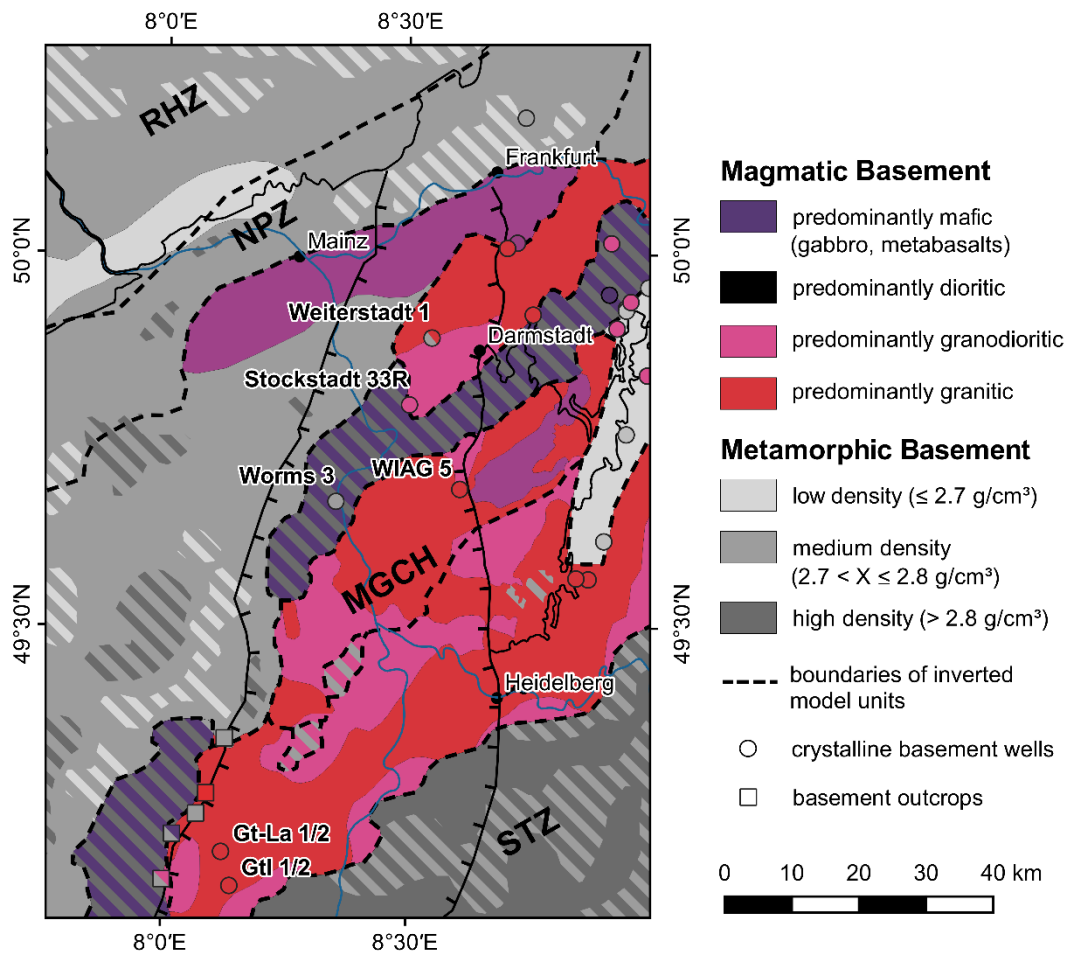
653 The petrophysical analysis revealed that the rock density and magnetic susceptibility are
654 strongly depending on the lithology (Tab. 2). Conversely, information on the distribution of the
655 main lithologies in the crystalline basement of the northern URG can be deduced from the
656 inverted parameter models (Fig. 9). Based on the outcrops at the graben margins, the deep
657 crystalline wells in the URG, and the density and susceptibility models, an interpretive geologic
658 map of the basement beneath the sedimentary cover was generated. (Fig. 11). Areas with
659 comparatively low magnetic susceptibility ($< 10^{-3}$ [SI]) are interpreted as being predominantly
660 metamorphic. This assumption can be confirmed in the Northern Phyllite Zone, the
661 Rhenohercynian Zone, and the Saxothuringian Zone, whose composition is relatively well
662 known from outcrops. It is also suggested that metamorphic rocks are dominant in the
663 northwestern MGCH, which is supported by exposed early Paleozoic metasediments in the
664 Palatinate and the petrophysical similarities to the Saxothuringian and Northern Phyllite Zone.
665 The transition between the metamorphic MGCH to the Northern Phyllite Zone is not marked

666 by a sharp discontinuity in the residual gravity signal, indicating major lithological parallels and
667 a paired evolution of these units in a volcanic arc respectively fore-arc setting (Krohe, 1991).

668 Large parts of the northern URG basement and the area east of it are presumably dominated
669 by plutonic rocks given the high magnetic susceptibility. The distinction between different
670 magmatic rocks is primarily based on the rock density (Tab. 2). According to this, granites and
671 granodiorites occur mainly in the southwestern extension of the Flasergranitoid Zone and in
672 the southern Bergsträßer Odenwald. The boundary between these two units cannot be clearly
673 traced in the density model, but the Flasergranitoid Zone is generally characterized by lower
674 susceptibility or, alternatively, increased remanent magnetization. Mafic rocks are
675 concentrated in a NNE-SSW trending band that includes the Southwestern Magnetic Body and
676 the Frankenstein Complex. Intermediate rocks may be present along the northern margin of
677 the MGCH, supported by the two wells Neuhof 1 and 2 encountering diorite.

678 The interpretation covers only the larger geological bodies, small-scale lithological variations
679 cannot be resolved with the applied method so far. Example for this are the narrow amphibolite-
680 gneiss complexes, the so-called Schieferzüge, in the Bergsträßer Odenwald, which are most
681 likely continuous towards the southwest. Their location in the northern URG can only be
682 estimated by assuming a constant strike direction. Furthermore, the natural variations of the
683 petrophysical parameters as well as the partial overlap of the parameter distributions of
684 different rock types imply considerable uncertainties in the separation of individual lithologies.
685 Also, in addition to the main rock type, density and magnetic susceptibility depend on several
686 aspects such as fracture porosity, hydrothermal alteration or mineral alteration (Airo, 2002;
687 Ladygin et al., 2000; Ündül, 2016), which cannot be quantified here in detail due to the lack of
688 comprehensive well data.

689 Despite the significant uncertainties, the presented investigations provide an important basis
690 for geothermal potential assessments in the northern URG. As mentioned above, especially
691 thermal but also hydraulic parameters are strongly affected by the lithology (Stober and
692 Bucher, 2007). Granitoids, which are the crystalline rocks with the most favorable properties
693 for geothermal exploitation, represent more than 50% of the basement in the northern URG.
694 In comparison, the less suitable mafic and metamorphic rocks occupy a rather subordinate
695 area. Additionally, Weinert et al. (2020a) found a direct relationship between bulk density and
696 thermal conductivity for the rock samples of the MGCH. The petrophysical models can
697 therefore be used to infer the spatial distribution of thermal properties in the basement, allowing
698 again more realistic potential estimates and heat flow simulations.



699

700 Figure 11: Interpretative map of the lithologies at the top basement based on the results of the joint gravity and
 701 magnetic inversion. Available crystalline basement wells and outcrops at the graben shoulders are largely
 702 consistent with the interpretation. RHZ = Rhenohercynian Zone, NPZ = Northern Phyllite Zone, MGCH = Mid-
 703 German Crystalline High, STZ = Saxothuringian Zone, URG = Upper Rhine Graben.

704 5.3 Geodynamic Interpretation

705 The MGCH is traditionally regarded as a volcanic arc or active continental margin, which was
 706 formed in the Late Devonian and Carboniferous by the southward subduction of the Rheic and
 707 Rhenohercynian Oceans and later continental collision (Franke, 2000; Kroner et al., 2008; Zeh
 708 and Gerdes, 2010). Due to contrasting geodynamic conditions along the strike direction, a
 709 zone of variable composition and structure has formed. Especially on the opposite sides of the
 710 URG, there are significant differences, mainly due to oblique convergence (Flöttmann and
 711 Oncken, 1992; Oncken, 1997). Accordingly, the MGCH is probably dominated by a
 712 metamorphic basement in the west, which can be interpreted as the relic of a Paleozoic fore-
 713 arc. East of the URG, the convergence rates during the main orogeny phase were much higher,
 714 therefore the fore-arc is not preserved in this area. Instead, subduction-related plutons and
 715 metamorphic rocks with pressure-dominated overprint are present here.

716 The Frankenstein Complex and Southwestern Magnetic Body are likely the remains of a
717 volcanic island arc (e.g. Altherr et al., 1999), which was formed in an early phase of the marine
718 basin closure. Whereas the basement is largely exposed in the Odenwald, it is covered by
719 Carboniferous to Triassic (meta-)sediments in the Palatinate. It appears that these two units
720 are separated by a 15 to 20 km sinistral offset near the western graben boundary fault. This
721 observation might be attributed to the sinistral strike-slip movements in the URG, which are
722 particularly evident in the central and southern rift valley. Alternatively, this setting might still
723 represent the primary geometry of the Variscan orogen with a changing trend from NE-SW in
724 the Odenwald to NNE-SSW in the Palatinate and Vosges.

725 6 Conclusions and Outlook

726 All publicly available structural and petrophysical data on the crystalline basement in the
727 northern URG were compiled into one comprehensive model. By integrating gravity and
728 magnetic data, a detailed geological 3D model of the region was developed. From the
729 investigations described above, the following conclusions can be drawn:

- 730 • Residual Bouguer and magnetic anomalies exhibit NE-SW oriented features that depict
731 the main Variscan basement structures. The metamorphic units are usually recognized
732 by gravity highs and magnetic lows, whereas the magmatic complexes are often
733 associated with magnetic highs and varying gravity anomalies.
- 734 • Joint inversion modelling allowed to obtain a density and susceptibility model of the
735 crystalline basement in the northern URG region which provides a good match with the
736 observed gravity and magnetic data
- 737 • The petrophysical analysis demonstrated that the main rock types are characterized by
738 specific properties. The inversion results can therefore be used to draw up an
739 interpretative map of the basement lithology in the northern URG, which is also
740 consistent with outcrops and wells.
- 741 • Major parts of the northern URG basement are dominated by granitoid intrusions that
742 offer suitable properties for deep geothermal utilization. Metamorphic and mafic rocks
743 are concentrated in a relatively narrow band and along the western graben border.
744 However, it must be mentioned that this interpretation remains speculative due to the
745 non-uniqueness of potential fields studies. Besides, only larger connected bodies can
746 be resolved; investigation of small-scale lithologic variations is not possible based on
747 the currently available data.

748 In the future studies, efforts will be focused on using the developed 3D model to perform a
749 most realistic estimation of the geothermal potential in the northern URG. The spatial

750 distribution of thermal properties can be derived from the inverted density model. Furthermore,
751 comprehensive structural geological information will be integrated, mainly from the Odenwald,
752 to assess the hydraulic properties of the basement.

753 To reduce the uncertainties related to the Permo-Carboniferous and Cenozoic volcanics, a
754 detailed analysis of well data from the northernmost URG, the Saar-Nahe Basin and the
755 Spredlinger Horst is necessary. In particular, the incorporation of all existing well logs would
756 improve the understanding of the location, thickness and properties of these horizons. In
757 addition, the joint inversion of gravitational and magnetic data is also promising on a smaller
758 scale, since a higher resolution of the discretized model would allow to map the properties of
759 large fault zones, which represent the main target for geothermal projects in the URG. For this
760 purpose, the integration of existing 3D seismic data sets, that allow a precise modelling of the
761 geological structures, seems promising. This would minimize the uncertainties of the forward
762 model considerably and the inversion could provide more reliable results.

763 Acknowledgements

764 We thank all researchers and involved institutions (TUDa, GFZ, HLNUG, LGRB-BW, LGB-RP)
765 of the Hessen 3D (1.0 and 2.0) and GeORG projects, whose activities were essential for this
766 study. We are furthermore grateful that the Institut für Steinkonservierung Mainz e.V. provided
767 the rock samples of the URG region for our petrophysical investigations. We thank Prof. Dr.
768 Eva Schill for the helpful discussions on the analysis and interpretation of the geophysical data.
769 Additionally, we thank Dr. Jens Grimmer and one anonymous reviewer for their critical but
770 constructive reviews and comments which helped to improve the manuscript considerably.

771 Funding

772 This study was funded by the Interreg NWE Program through the Roll-out of Deep Geothermal
773 Energy in North-West Europe (DGE-ROLLOUT) Project (www.nweurope.eu/DGE-Rollout).
774 The Interreg NWE Program is part of the European Cohesion Policy and is financed by the
775 European Regional Development Fund (ERDF).

776 Data Availability Statement

777 Datasets containing petrophysical properties of the crystalline basement in the URG region
778 including density and magnetic susceptibility measurements can be found at
779 <https://doi.org/10.5194/essd-12-2485-2020> (Bär et al., 2020),
780 <https://doi.org/10.25534/tudatalib-278> (Weinert et al., 2020b) and
781 <https://doi.org/10.48328/tudatalib-393> (Frey et al., 2020). Gravity and magnetic data can be

782 requested individually from the Leibniz Institute for Applied Geophysics (LIAG), the Hessian
783 Administration for Soil Management and Geoinformation (HVBG) and the State Agency for
784 Surveying and Geo Base Information Rhineland-Palatinate (LVermGeo). Finally, the 3D model
785 of the northern URG crystalline basement is publicly available at
786 <https://doi.org/10.48328/tudatalib-417.2> (Frey et al., 2021).

787 References

- 788 Agemar, T., Schellschmidt, R., Schulz, R., 2012. Subsurface Temperature Distribution of
789 Germany. *Geothermics* 44, 65–77. <https://doi.org/10.1016/j.geothermics.2012.07.002>.
- 790 Airo, M.-L., 2002. Aeromagnetic And Aeroradiometric Response To Hydrothermal Alteration.
791 *Surveys in Geophysics* 23, 273–302. <https://doi.org/10.1023/A:1015556614694>.
- 792 Altenberger, U., Besch, T., 1993. The Bllstein Odenwald: evidence for pre- to early Variscan
793 plate convergence in the Central European variscides. *International Journal of Earth*
794 *Sciences* 82 (3), 475–488. <https://doi.org/10.1007/BF00212411>.
- 795 Altherr, R., Henes-Klaiber, U., Hegner, E., Satir, M., Langer, C., 1999. Plutonism in the
796 Variscan Odenwald (Germany): from subduction to collision. *International Journal of*
797 *Earth Sciences* 88, 422–443. <https://doi.org/10.1007/s005310050276>.
- 798 Anderle, H.-J., Franke, W., Schwab, M., 1995. III.C.1 Stratigraphy, in: Dallmeyer, R.D.,
799 Franke, W., Weber, K. (Eds.), *Pre-Permian Geology of Central and Eastern Europe*.
800 Springer Berlin Heidelberg, Berlin, Heidelberg, pp. 99–107.
- 801 Anthes, G., Reischmann, T., 1997. New 207Pb/206Pb single zircon evaporation ages from
802 the central part of the Mid German Crystalline Rise. *Terra Nostra* 97 (5), 10.
803 <https://doi.org/10.1016/j.jseae.2007.04.004>.
- 804 Aretz, A., Bär, K., Götz, A.E., Sass, I., 2016. Outcrop analogue study of Permocarboniferous
805 geothermal sandstone reservoir formations (northern Upper Rhine Graben, Germany):
806 impact of mineral content, depositional environment and diagenesis on petrophysical
807 properties. *International Journal of Earth Sciences* 105 (5), 1431–1452.
808 <https://doi.org/10.1007/s00531-015-1263-2>.
- 809 Arndt, D., 2012. Geologische Strukturmodellierung von Hessen zur Bestimmung von
810 Geopotenzialen. Dissertation, Technical University of Darmstadt, 116 pp.
- 811 Bächler, D., Kohl, T., Rybach, L., 2003. Impact of graben-parallel faults on hydrothermal
812 convection—Rhine Graben case study. *Physics and Chemistry of the Earth, Parts A/B/C*
813 28, 431–441. [https://doi.org/10.1016/S1474-7065\(03\)00063-9](https://doi.org/10.1016/S1474-7065(03)00063-9).
- 814 Backhaus, E., 1974. Limnische und fluviatile Sedimentation im südwestdeutschen
815 Buntsandstein. *International Journal of Earth Sciences* 63 (3), 925–942.
816 <https://doi.org/10.1007/BF01821318>.
- 817 Backhaus, E., 1975. Der Buntsandstein im Odenwald, in: Amstutz, G.C., Meisl, S., Nickel, E.
818 (Eds.), *Mineralien und Gesteine im Odenwald*. Heidelberg, pp. 299–320.
- 819 Backhaus, E., Heim, D., 1995. Die fluvio-lakustrine Fazies des Übergangsbereichs
820 Plattensandstein/Rötquarzit (Oberer Buntsandstein) im mittleren Odenwald unter
821 besonderer Berücksichtigung der Violetten Zone. *Geol. Jb. Hessen* 123, 49–68.
- 822 Backhaus, E., Schwarz, S., 2003. Ein Sammelprofil des Buntsandsteins und Zechsteins im
823 mittleren Odenwald anhand von Bohrungen und Gamma-Logs. *Geol. Jb. Hessen* 130,
824 91–107.

825 Baillieux, P., Schill, E., Edel, J.-B., Mauri, G., 2013. Localization of temperature anomalies in
826 the Upper Rhine Graben: insights from geophysics and neotectonic activity. *International*
827 *Geology Review* 55 (14), 1744–1762. <https://doi.org/10.1080/00206814.2013.794914>.

828 Bär, K.M., 2012. Untersuchung der tiefengeothermischen Potenziale von Hessen.
829 Dissertation, Technical University of Darmstadt, 268 pp.

830 Bär, K., Hintze, M., Weinert, S., Sippel, J., Freymark, J., Scheck-Wenderoth, M., Sass, I.,
831 2016. Das Verbundprojekt Hessen 3D 2.0. *Geothermische Energie* 3 (85), 24–25.

832 Bär, K., Reinsch, T., Bott, J., 2020. The PetroPhysical Property Database (P³) – a global
833 compilation of lab-measured rock properties. *Earth Syst. Sci. Data* 12 (4), 2485–2515.
834 <https://doi.org/10.5194/essd-12-2485-2020>.

835 Bär, K., Homuth, B., Stiller, M., Weinert, S., Bott, J., Oncken, O., Franke, W., Henke, A.,
836 2021, in prep. New Interpretation of a reprocessed Crustal Scale Seismic Profile across
837 the Mid German Crystalline High and the Northern Upper Rhine Graben, Germany. In
838 preparation for *Geochemistry, Geophysics, Geosystems*, AGU Advancing Earth and
839 Space Science Journal.

840 Behr, H.-J., Engel, W., Franke, W., Giese, P., Weber, K., 1984. The Variscan Belt in Central
841 Europe: Main structures, geodynamic implications, open questions. *Tectonophysics* 109
842 (1-2), 15–40. [https://doi.org/10.1016/0040-1951\(84\)90168-9](https://doi.org/10.1016/0040-1951(84)90168-9).

843 Behr, H.J., Heinrichs, T., 1987. Geological interpretation of DEKORP 2-S: A deep seismic
844 reflection profile across the Saxothuringian and possible implications for the Late
845 Variscan structural evolution of Central Europe. *Tectonophysics* 142 (2-4), 173–202.
846 [https://doi.org/10.1016/0040-1951\(87\)90122-3](https://doi.org/10.1016/0040-1951(87)90122-3).

847 Behrmann, J.H., Hermann, O., Horstmann, M., Tanner, D.C., Bertrand, G., 2003. Anatomy
848 and kinematics of oblique continental rifting revealed: A three-dimensional case study of
849 the southeast Upper Rhine graben (Germany). *Bulletin* 87 (7), 1105–1121.
850 <https://doi.org/10.1306/02180300153>.

851 Böcker, J., 2015. Petroleum system and thermal history of the Upper Rhine Graben -
852 Implications from organic geochemical analyses, oil-source rock correlations and
853 numerical modelling. Dissertation, RWTH Aachen, 154 pp.

854 Boigk, H., Schöneich, H., 1974. The Rhinegraben: geologic history and neotectonic activity –
855 Perm, Trias und älterer Jura im Bereich der südlichen Mittelmeer-Mjösen-Zone und des
856 Rheingrabens, in: Illies, J.H., Fuchs, K. (Eds.), *Approaches to Taphrogenesis*.
857 Schweizerbart, Stuttgart, pp. 60–72.

858 Boigk, H., 1981. *Erdöl und Erdölgas in der Bundesrepublik Deutschland*. Schweizerbart,
859 Stuttgart, 330 pp.

860 Bosch, M., McGaughey, J., 2001. Joint inversion of gravity and magnetic data under
861 lithologic constraints. *The Leading Edge* 20 (8), 877–881.
862 <https://doi.org/10.1190/1.1487299>.

863 Bosch, M., Meza, R., Jiménez, R., Hönig, A., 2006. Joint gravity and magnetic inversion in
864 3D using Monte Carlo methods. *GEOPHYSICS* 71 (4), G153-G156.
865 <https://doi.org/10.1190/1.2209952>.

866 Brun, J.P., Gutscher, M.-A., teams, 1992. Deep crustal structure of the Rhine Graben from
867 dekorp-ecors seismic reflection data: A summary. *Tectonophysics* 208 (1-3), 139–147.
868 [https://doi.org/10.1016/0040-1951\(92\)90340-C](https://doi.org/10.1016/0040-1951(92)90340-C).

869 Buchmann, T.J., Connolly, P.T., 2007. Contemporary kinematics of the Upper Rhine Graben:
870 A 3D finite element approach. *Global and Planetary Change* 58, 287–309.
871 <https://doi.org/10.1016/j.gloplacha.2007.02.012>.

- 872 Buchner, F., 1981. Rhinegraben: Horizontal stylolites indicating stress regimes of earlier
873 stages of rifting. *Tectonophysics* 73 (1-3), 113–118. [https://doi.org/10.1016/0040-
874 1951\(81\)90178-5](https://doi.org/10.1016/0040-1951(81)90178-5).
- 875 Calcagno, P., Chilès, J.P., Courrioux, G., Guillen, A., 2008. Geological modelling from field
876 data and geological knowledge, Part I – Modelling method coupling 3D potential-field
877 interpolation and geological rules. *Physics of the Earth and Planetary Interiors* 171 (1-4),
878 147–157. <https://doi.org/10.1016/j.pepi.2008.06.013>.
- 879 Crowley, Q.G., Floyd, P.A., Winchester, J.A., Franke, W., Holland, J.G., 2000. Early
880 Palaeozoic rift-related magmatism in Variscan Europe: fragmentation of the Armorican
881 Terrane Assemblage. *Terra Nova* 12 (4), 171–180. [https://doi.org/10.1046/j.1365-
882 3121.2000.00290.x](https://doi.org/10.1046/j.1365-3121.2000.00290.x).
- 883 Dachroth, W., 1988. Genese des linksrheinischen Buntsandsteins und Beziehungen
884 zwischen Ablagerungsbedingungen und Stratigraphie. *Jahresberichte und Mitteilungen
885 des Oberrheinischen Geologischen Vereins* 70, 267–333.
886 <https://doi.org/10.1127/jmoqv/70/1988/267>.
- 887 Dallmeyer, R.D., Franke, W., Weber, K. (Eds.), 1995. *Pre-Permian Geology of Central and
888 Eastern Europe*. Springer Berlin Heidelberg, Berlin, Heidelberg, 593 pp.
- 889 Dezayes, C., Lerouge, C., Innocent, C., Lach, P., 2021. Structural control on fluid circulation
890 in a graben system: Constraints from the Saint Pierre Bois quarry (Vosges, France).
891 *Journal of Structural Geology* 146, 104323. <https://doi.org/10.1016/j.jsg.2021.104323>.
- 892 Dèzes, P., Schmid, S.M., Ziegler, P.A., 2004. Evolution of the European Cenozoic Rift
893 System: interaction of the Alpine and Pyrenean orogens with their foreland lithosphere.
894 *Tectonophysics* 389 (1-2), 1–33. <https://doi.org/10.1016/j.tecto.2004.06.011>.
- 895 DoebI, F., 1967. The Tertiary and Pleistocene sediments of the northern and central part of
896 the Upper Rhinegraben. *Abhandlungen des Geologischen Landesamtes Baden-
897 Württemberg* 6, 48–54.
- 898 DoebI, F., Olbrecht, W., 1974. An isobath map of the Tertiary base in the Rhinegraben, in:
899 Illies, J.H., Fuchs, K. (Eds.), *Approaches to Taphrogenesis*. Schweizerbart, Stuttgart,
900 pp. 71–72.
- 901 Edel, J.B., Fluck, P., 1989. The upper Rhenish Shield basement (Vosges, Upper
902 Rhinegraben and Schwarzwald): Main structural features deduced from magnetic,
903 gravimetric and geological data. *Tectonophysics* 169 (4), 303–316.
904 [https://doi.org/10.1016/0040-1951\(89\)90093-0](https://doi.org/10.1016/0040-1951(89)90093-0).
- 905 Edel, J.B., Weber, K., 1995. Cadomian terranes, wrench faulting and thrusting in the central
906 Europe Variscides: geophysical and geological evidence. *International Journal of Earth
907 Sciences* 84. <https://doi.org/10.1007/BF00260450>.
- 908 Edel, J.-B., Schulmann, K., Rotstein, Y., 2007. The Variscan tectonic inheritance of the
909 Upper Rhine Graben: evidence of reactivations in the Lias, Late Eocene–Oligocene up to
910 the recent. *International Journal of Earth Sciences* 96, 305–325.
911 <https://doi.org/10.1007/s00531-006-0092-8>.
- 912 Edel, J., Schulmann, K., 2009. Geophysical constraints and model of the “Saxothuringian
913 and Rhenohercynian subductions - magmatic arc system” in NE France and SW
914 Germany. *Bulletin De La Societe Geologique De France - BULL SOC GEOL FR* 180,
915 545–558. <https://doi.org/10.2113/gssgfbull.180.6.545>.
- 916 Edel, J.B., Maurer, V., Dalmais, E., Genter, A., Richard, A., Letourneau, O., Hehn, R., 2018.
917 Structure and nature of the Palaeozoic basement based on magnetic, gravimetric and
918 seismic investigations in the central Upper Rhinegraben. *Geothermal Energy* 6 (1), 13.
919 <https://doi.org/10.1186/s40517-018-0099-y>.

920 Feist-Burkhardt, S., Götz, A., Szulc, J., Borkhataria, R., Geluk, M., Haas, J., Hornung, J.,
921 Jordan, P., Kempf, O., Jozef, M., Nawrocki, J., Reinhardt, L., Ricken, W., Röhling, H.-G.,
922 Ruffer, T., Török, Á., Zuehlke, R., 2008. Triassic, in: McCann, T. (Ed.), *The Geology of*
923 *Central Europe: Volume 2: Mesozoic and Cenozoic*. Geological Society of London,
924 London, pp. 749–821.

925 Flöttmann, T., Oncken, O., 1992. Constraints on the evolution of the Mid German Crystalline
926 Rise - a study of outcrops west of the river Rhine. *Geologische Rundschau* 82 (2), 515–
927 543.

928 Franke, W., 2000. The mid-European segment of the Variscides: tectonostratigraphic units,
929 terrane boundaries and plate tectonic evolution. Geological Society, London, Special
930 Publications 179, 35–61. <https://doi.org/10.1144/GSL.SP.2000.179.01.05>.

931 Franke, W., Cocks, L.R.M., Torsvik, T.H., 2017. The Palaeozoic Variscan oceans revisited.
932 *Gondwana Research* 48, 257–284. <https://doi.org/10.1016/j.gr.2017.03.005>.

933 Frenzel, G., 1971. Die Mineralparagenese der Albersweiler Lamprophyre. *Neues J. Mineral.*
934 *Abh.* 115, 164–191.

935 Frey, M., Bär, K., Sass, I., 2020. Database of the Magnetic Susceptibility of the Mid-German
936 Crystalline High. Technical University of Darmstadt. TUdataLib.
937 <https://doi.org/10.48328/tudatalib-393>.

938 Frey, M., Ebbing, J., 2020. The deep geothermal potential of the radiogenic Løvstakken
939 Granite in western Norway. *NJG*. <https://doi.org/10.17850/njg100-1-4>.

940 Freymark, J., Sippel, J., Scheck-Wenderoth, M., Baer, K., Stiller, M., Kracht, M., Fritsche, J.-
941 G., 2015. Heterogeneous Crystalline Crust Controls the Shallow Thermal Field – A Case
942 Study of Hessen (Germany). *Energy Procedia* 76, 331–340.
943 <https://doi.org/10.1016/j.egypro.2015.07.837>.

944 Freymark, J., Sippel, J., Scheck-Wenderoth, M., Bär, K., Stiller, M., Fritsche, J.-G., Kracht,
945 M., 2017. The deep thermal field of the Upper Rhine Graben. *Tectonophysics* 694, 114–
946 129. <https://doi.org/10.1016/j.tecto.2016.11.013>.

947 Freymark, J., Bott, J., Scheck-Wenderoth, M., Bär, K., Stiller, M., Fritsche, J.-G., Kracht, M.,
948 Gomez Dacal, M.L., 2020. 3D-URG: 3D gravity constrained structural model of the Upper
949 Rhine Graben. *GFZ Data Services*. <https://doi.org/10.5880/GFZ.4.5.2020.004>.

950 Gabriel, G., Vogel, D., Scheibe, R., Lindner, H., Pucher, R., Wonik, T., Krawczyk, C.M.,
951 2011. Anomalies of the Earth's total magnetic field in Germany – the first complete
952 homogenous data set reveals new opportunities for multiscale geoscientific studies.
953 *Geophys J Int* 184 (3), 1113–1118. <https://doi.org/10.1111/j.1365-246X.2010.04924.x>.

954 Gallardo, L.A., Thebaud, N., 2012. New insights into Archean granite-greenstone architecture
955 through joint gravity and magnetic inversion. *Geology* 40 (3), 215–218.
956 <https://doi.org/10.1130/G32817.1>.

957 Geyer, O.F., Gwinner, M.P., Simon, T., 2011. *Geologie von Baden-Württemberg*, 5th ed.
958 Schweizerbart, Stuttgart, 627 pp.

959 Giese, P., 1995. Main Features of Geophysical Structures in Central Europe, in: Dallmeyer,
960 R.D., Franke, W., Weber, K. (Eds.), *Pre-Permian Geology of Central and Eastern Europe*.
961 Springer Berlin Heidelberg, Berlin, Heidelberg, pp. 7–25.

962 Grimmer, J.C., Ritter, J.R.R., Eisbacher, G.H., Fielitz, W., 2017. The Late Variscan control on
963 the location and asymmetry of the Upper Rhine Graben. *International Journal of Earth*
964 *Sciences* 106 (3), 827–853. <https://doi.org/10.1007/s00531-016-1336-x>.

965 Guillen, A., Calcagno, P., Courrioux, G., Joly, A., Ledru, P., 2008. Geological modelling from
966 field data and geological knowledge, Part II, Modelling validation using gravity and
967 magnetic data inversion. *Physics of the Earth and Planetary Interiors* 171 (1-4), 158–169.
968 <https://doi.org/10.1016/j.pepi.2008.06.014>.

- 969 Hammer, S., 1963. Deep Gravity Interpretation by Stripping. *GEOPHYSICS* 28 (3), 369–378.
 970 <https://doi.org/10.1190/1.1439186>.
- 971 Henk, A., 1992. Mächtigkeit und Alter der erodierten Sedimente im Saar-Nahe-Becken (SW-
 972 Deutschland). *International Journal of Earth Sciences* 81 (2), 323–331.
 973 <https://doi.org/10.1007/BF01828601>.
- 974 Henk, A., 1993a. Late orogenic Basin evolution in the Variscan internides: the Saar-Nahe
 975 Basin, southwest Germany. *Tectonophysics* 223 (3-4), 273–290.
 976 [https://doi.org/10.1016/0040-1951\(93\)90141-6](https://doi.org/10.1016/0040-1951(93)90141-6).
- 977 Henk, A., 1993b. Subsidenz und tektonik des Saar-Nahe-Beckens (SW-Deutschland).
 978 *International Journal of Earth Sciences* 82 (1), 3–19. <https://doi.org/10.1007/BF00563266>.
- 979 Hertle, M., 2003. Numerische Simulation der geologischen Entwicklungsgeschichte des
 980 permokarbonen Saar-Nahe-Beckens. Dissertation, RWTH Aachen, 166 pp.
- 981 Hirschmann, G., 1995. IV.B Lithological Characteristics, in: Dallmeyer, R.D., Franke, W.,
 982 Weber, K. (Eds.), *Pre-Permian Geology of Central and Eastern Europe*. Springer Berlin
 983 Heidelberg, Berlin, Heidelberg, pp. 155–163.
- 984 Homuth, B., Rumpker, G., Deckert, H., Kracht, M., 2014. Seismicity of the northern Upper
 985 Rhine Graben — Constraints on the present-day stress field from focal mechanisms.
 986 *Tectonophysics* 632, 8–20. <https://doi.org/10.1016/j.tecto.2014.05.037>.
- 987 Illies, J.H., Greiner, G., 1979. Holocene Movements and State of Stress in the Rhinegraben
 988 Rift System 13, 349–359. <https://doi.org/10.1016/B978-0-444-41783-1.50057-X>.
- 989 Intrepid Geophysics, 2017. *GeoModeller User Manual: Tutorial C (Forward & Inverse
 990 Modelling of Potential Fields)*.
- 991 Jain, C., Vogt, C., Clauser, C., 2015. Maximum potential for geothermal power in Germany
 992 based on engineered geothermal systems. *Geotherm Energy* 3 (1).
 993 <https://doi.org/10.1186/s40517-015-0033-5>.
- 994 Jaupart, C., Mareschal, J.-C., Jarosky, L., 2016. Radiogenic heat production in the
 995 continental crust. *Lithos* 262, 398–427. <https://doi.org/10.1016/j.lithos.2016.07.017>.
- 996 Jodocy, M., Stober, I., 2010. Geologisch-geothermische Tiefenprofile für den südlichen Teil
 997 des Oberrheingrabens in Baden-Württemberg. *Z. geol. Wiss.* 38 (1), 3–25.
- 998 Kamm, J., Lundin, I.A., Bastani, M., Sadeghi, M., Pedersen, L.B., 2015. Joint inversion of
 999 gravity, magnetic, and petrophysical data — A case study from a gabbro intrusion in
 1000 Boden, Sweden. *GEOPHYSICS* 80 (5), B131-B152. <https://doi.org/10.1190/geo2014-0122.1>.
- 1001
- 1002 Kemnitz, H., Romer, R.L., Oncken, O., 2002. Gondwana break-up and the northern margin of
 1003 the Saxothuringian belt (Variscides of Central Europe). *International Journal of Earth
 1004 Sciences* 91 (2), 246–259. <https://doi.org/10.1007/s005310100209>.
- 1005 Kirsch, H., Kober, B., Lippolt, H.J., 1988. Age of intrusion and rapid cooling of the
 1006 Frankenstein gabbro (Odenwald, SW-Germany) evidenced by $^{40}\text{Ar}/^{39}\text{Ar}$ and single-
 1007 zircon $^{207}\text{Pb}/^{206}\text{Pb}$ measurements. *International Journal of Earth Sciences* 77 (3), 693–
 1008 711. <https://doi.org/10.1007/BF01830178>.
- 1009 Klügel, T., 1997. Geometrie und Kinematik einer variszischen Plattengrenze: der Südrand
 1010 des Rhenoherynikums im Taunus. *Hessisches Landesamt für Bodenforschung*, 215 pp.
- 1011 Kossmat, F., 1927. Gliederung des varistischen Gebirgsbaues: *Abhandlungen Sächsischen
 1012 Geologischen Landesamts*, v. 1.
- 1013 Kreuzer, H., Harre, W., 1975. K/Ar-Altersbestimmungen an Hornblenden und Biotiten des
 1014 Kristallinen Odenwalds, in: Amstutz, G.C., Meisl, S., Nickel, E. (Eds.), *Mineralien und
 1015 Gesteine im Odenwald*. Heidelberg, pp. 70–78.

- 1016 Krohe, A., 1991. Emplacement of synkinematic plutons in the Variscan Odenwald (Germany)
1017 controlled by transtensional tectonics. *International Journal of Earth Sciences* 80 (2),
1018 391–409. <https://doi.org/10.1007/BF01829373>.
- 1019 Krohe, A., 1992. Structural evolution of intermediate-crustal rocks in a strike-slip and
1020 extensional setting (Variscan Odenwald, SW Germany): differential upward transport of
1021 metamorphic complexes and changing deformation mechanisms. *Tectonophysics* 205
1022 (4), 357–386. [https://doi.org/10.1016/0040-1951\(92\)90443-A](https://doi.org/10.1016/0040-1951(92)90443-A).
- 1023 Krohe, A., Willner, A.P., 1995. IV.C.2 The Odenwald Crystalline Complex, in: Dallmeyer,
1024 R.D., Franke, W., Weber, K. (Eds.), *Pre-Permian Geology of Central and Eastern Europe*.
1025 Springer Berlin Heidelberg, Berlin, Heidelberg, pp. 182–185.
- 1026 Kroner, U., Mansy, J.L., Mazur, S., Aleksandrowski, P., Hann, H.P., Huckriede, H., 2008.
1027 Variscan tectonics, in: McCann, T. (Ed.), *The Geology of Central Europe: Volume 1:*
1028 *Precambrian and Palaeozoic*. Geological Society of London, London, pp. 599–664.
- 1029 Lachenbruch, A.H., 1970. Crustal temperature and heat production: Implications of the linear
1030 heat-flow relation. *J. Geophys. Res.* 75 (17), 3291–3300.
1031 <https://doi.org/10.1029/JB075i017p03291>.
- 1032 Ladygin, V., Frolova, J., Rychagov, S., 2000. Formation of composition and petrophysical
1033 properties of hydrothermally altered rocks in geothermal reservoir. *Proc. WGC*, 2695–
1034 2699.
- 1035 Lajaunie, C., Courrioux, G., Manuel, L., 1997. Foliation fields and 3D cartography in geology:
1036 Principles of a method based on potential interpolation. *Math Geol* 29 (4), 571–584.
1037 <https://doi.org/10.1007/BF02775087>.
- 1038 Laue, S., Reischmann, T., Emmermann, K.H., 1990. Geochemical variation of granitoid rocks
1039 from the NW margin of the Rhinegraben. *Ber Dsch Mineral Ges Eur J Mineral* 2 (Beih 1),
1040 156.
- 1041 Laue, S., Reischmann, T., 1994. Petrographie und Geochemie variszischer Intrusiva der
1042 westlichen Rheingrabenschulter. *Mitt Pollichia* 81, 195–214.
- 1043 Li, Y., Oldenburg, D.W., 1996. 3-D inversion of magnetic data. *GEOPHYSICS* 61 (2), 394–
1044 408. <https://doi.org/10.1190/1.1443968>.
- 1045 Li, Y., Oldenburg, D.W., 1998. 3-D inversion of gravity data. *GEOPHYSICS* 63 (1), 109–119.
1046 <https://doi.org/10.1190/1.1444302>.
- 1047 Marell, D., 1989. *Das Rotliegende zwischen Odenwald und Taunus*. Geologische
1048 *Abhandlungen Hessen*, Wiesbaden.
- 1049 Mareschal, J.-C., Jaupart, C., 2013. Radiogenic heat production, thermal regime and
1050 evolution of continental crust. *Tectonophysics* 609, 524–534.
1051 <https://doi.org/10.1016/j.tecto.2012.12.001>.
- 1052 Martha, S.O., Zulauf, G., Dörr, W., Nesbor, H.-D., Petschick, R., Prinz-Grimm, P., Gerdes, A.,
1053 2014. The Saxothuringian-Rhenohercynian boundary underneath the Vogelsberg
1054 volcanic field: evidence from basement xenoliths and U-Pb zircon data of trachyte. *zdgg*
1055 165, 373–394. <https://doi.org/10.1127/1860-1804/2014/0079>.
- 1056 McCann, T. (Ed.), 2008a. *The Geology of Central Europe: Volume 1: Precambrian and*
1057 *Palaeozoic*. Geological Society of London, London, 748 pp.
- 1058 McCann, T. (Ed.), 2008b. *The Geology of Central Europe: Volume 2: Mesozoic and*
1059 *Cenozoic*. Geological Society of London, London, 752 pp.
- 1060 McCann, T., Skompski, S., Poty, E., Dusar, M., Vojarova, A., Schneider, J., Wetzels, A.,
1061 Krainer, K., 2008. Carboniferous, in: McCann, T. (Ed.), *The Geology of Central Europe:*
1062 *Volume 1: Precambrian and Palaeozoic*. Geological Society of London, London, pp. 410–
1063 530.

- 1064 Meier, L., Eisbacher, G.H., 1991. Crustal kinematics and deep structure of the northern
 1065 Rhine Graben, Germany. *Tectonics* 10 (3), 621–630. <https://doi.org/10.1029/91TC00142>.
- 1066 Meissner, R., Bortfeld, R.K. (Eds.), 1990. DEKORP-Atlas: Results of Deutsches
 1067 Kontinentales Reflexionsseismisches Programm, 1st ed. Springer, Berlin.
- 1068 Molenaar, N., Felder, M., Bär, K., Götz, A.E., 2015. What classic greywacke (litharenite) can
 1069 reveal about feldspar diagenesis: An example from Permian Rotliegend sandstone in
 1070 Hessen, Germany. *Sedimentary Geology* 326, 79–93.
 1071 <https://doi.org/10.1016/j.sedgeo.2015.07.002>.
- 1072 Mosegaard, K., Tarantola, A., 1995. Monte Carlo sampling of solutions to inverse problems.
 1073 *J. Geophys. Res.* 100 (B7), 12431–12447. <https://doi.org/10.1029/94JB03097>.
- 1074 Müller, H., 1996. Das Permokarbon im nördlichen Oberrheingraben: Paläogeographische
 1075 und strukturelle Entwicklung des permokarbonen Saar-Nahe-Beckens im nördlichen
 1076 Oberrheingraben. Hess. Landesamt für Bodenforschung, Wiesbaden, 85 pp.
- 1077 Okrusch, M., 1995. Metamorphic Evolution, in: Dallmeyer, R.D., Franke, W., Weber, K.
 1078 (Eds.), *Pre-Permian Geology of Central and Eastern Europe*. Springer Berlin Heidelberg,
 1079 Berlin, Heidelberg, pp. 201–213.
- 1080 Okrusch, M., Schubert, W., Nasir, S., 1995. IV.D Igneous Activity (Pre- to Early Variscan
 1081 Magmatism), in: Dallmeyer, R.D., Franke, W., Weber, K. (Eds.), *Pre-Permian Geology of*
 1082 *Central and Eastern Europe*. Springer Berlin Heidelberg, Berlin, Heidelberg, pp. 190–200.
- 1083 Oncken, O., 1995. III.B.2 Structure, in: Dallmeyer, R.D., Franke, W., Weber, K. (Eds.), *Pre-*
 1084 *Permian Geology of Central and Eastern Europe*. Springer Berlin Heidelberg, Berlin,
 1085 Heidelberg, pp. 50–58.
- 1086 Oncken, O., 1997. Transformation of a magmatic arc and an orogenic root during oblique
 1087 collision and its consequences for the evolution of the European Variscides (Mid-German
 1088 Crystalline Rise). *Geologische Rundschau* 86 (1), 2–20.
 1089 <https://doi.org/10.1007/s005310050118>.
- 1090 Oncken, O., 1998. Orogenic mass transfer and reflection seismic patterns — evidence from
 1091 DEKORP sections across the European Variscides (central Germany). *Tectonophysics*
 1092 286, 47–61. [https://doi.org/10.1016/S0040-1951\(97\)00254-0](https://doi.org/10.1016/S0040-1951(97)00254-0).
- 1093 Oncken, O., Winterfeld, C. von, Dittmar, U., 1999. Accretion of a rifted passive margin: The
 1094 Late Paleozoic Rhenohercynian fold and thrust belt (Middle European Variscides).
 1095 *Tectonics* 18 (1), 75–91. <https://doi.org/10.1029/98TC02763>.
- 1096 Reinhold, C., Schwarz, M., Bruss, D., Heesbeen, B., Perner, M., Suana, M., 2016. The
 1097 Northern Upper Rhine Graben : re-dawn of a mature petroleum province? *Swiss Bull*
 1098 *angew. Geol.* 21, 35–56. <https://doi.org/10.5169/seals-658196>.
- 1099 Reischmann, T., Anthes, G., Jaeckel, P., Altenberger, U., 2001. Age and origin of the
 1100 Böllsteiner Odenwald. *Mineralogy and Petrology* 72 (1-3), 29–44.
 1101 <https://doi.org/10.1007/s007100170025>.
- 1102 Rotstein, Y., Edel, J.-B., Gabriel, G., Boulanger, D., Schaming, M., Munsch, M., 2006.
 1103 Insight into the structure of the Upper Rhine Graben and its basement from a new
 1104 compilation of Bouguer Gravity. *Tectonophysics* 425, 55–70.
 1105 <https://doi.org/10.1016/j.tecto.2006.07.002>.
- 1106 Rotstein, Y., Schaming, M., 2011. The Upper Rhine Graben (URG) revisited: Miocene
 1107 transtension and transpression account for the observed first-order structures. *Tectonics*
 1108 30, 1-14. <https://doi.org/10.1029/2010TC002767>.
- 1109 Rousset, D., Bayer, R., Guillon, D., Edel, J.B., 1993. Structure of the southern Rhine Graben
 1110 from gravity and reflection seismic data (ecors-dekorp program). *Tectonophysics* 221 (2),
 1111 135–153. [https://doi.org/10.1016/0040-1951\(93\)90329-l](https://doi.org/10.1016/0040-1951(93)90329-l).

- 1112 Schäfer, A., 1989. Variscan molasse in the Saar-Nahe Basin (W-Germany), Upper
 1113 Carboniferous and Lower Permian. *International Journal of Earth Sciences* 78 (2), 499–
 1114 524. <https://doi.org/10.1007/BF01776188>.
- 1115 Schäfer, A., 2011. Tectonics and sedimentation in the continental strike-slip Saar-Nahe Basin
 1116 (Carboniferous-Permian, West Germany). *zdg* 162 (2), 127–155.
 1117 <https://doi.org/10.1127/1860-1804/2011/0162-0127>.
- 1118 Scheck-Wenderoth, M., Krzywiec, P., Zühlke, R., Maystrenko, Y., Froitzheim, N., 2008.
 1119 Permian to Cretaceous tectonics of Central Europe, in: McCann, T. (Ed.), *The Geology of*
 1120 *Central Europe: Volume 1: Precambrian and Palaeozoic*. Geological Society of London,
 1121 London, pp. 999–1030.
- 1122 Schumacher, M.E., 2002. Upper Rhine Graben: Role of preexisting structures during rift
 1123 evolution. *Tectonics* 21 (1), 6-1-6-17. <https://doi.org/10.1029/2001TC900022>.
- 1124 Seckendorff, V. von, Arz, C., Lorenz, V., 2004. Magmatism of the late Variscan intermontane
 1125 Saar-Nahe Basin (Germany): a review. Geological Society, London, *Special Publications*
 1126 223 (1), 361–391. <https://doi.org/10.1144/GSL.SP.2004.223.01.16>.
- 1127 Sissingh, W., 1998. Comparative Tertiary stratigraphy of the Rhine Graben, Bresse Graben
 1128 and Molasse Basin: correlation of Alpine foreland events. *Tectonophysics* 300 (1-4), 249–
 1129 284. [https://doi.org/10.1016/S0040-1951\(98\)00243-1](https://doi.org/10.1016/S0040-1951(98)00243-1).
- 1130 Sittler, C., 1969. The sedimentary trough of the Rhine graben. *Tectonophysics* 8, 543–560.
- 1131 Sittler, C., 1992. Illustration de l'histoire géologique du Fossé rhénan et de l'Alsace. *Neues*
 1132 *Jahrb. für Geol. und Paläontologie Abhandlungen* 186 (3), 255–282.
- 1133 Skrzypek, E., Schulmann, K., Tabaud, A.-S., Edel, J.-B., 2014. Palaeozoic evolution of the
 1134 Variscan Vosges Mountains. Geological Society, London, *Special Publications* 405 (1),
 1135 45–75. <https://doi.org/10.1144/SP405.8>.
- 1136 Sokol, G., Nitsch, E., Anders, B., Beccaletto, L., Capar, L., Mermey, D.C., Dezayes, C.,
 1137 Dresmann, H., Elsass, P., Fehn, C., Fischer, G., Franz, M., Haneke, J., Huggenberger,
 1138 P., Kärcher, T., Krzyzanowski, J., Oliviero, G., Prestel, R., Rodat, C., Rupf, I., Schuff, J.,
 1139 Siemon, S., Storz, R., Tesch, J., Urban, S., Weidenfeller, M., Wielandt-Schuster, U.,
 1140 Wirsing, G., Zumsprekel, H., 2013. Geopotenziale des tieferen Untergrundes im
 1141 Oberrheingraben: Fachlich-Technischer Abschlussbericht des INTERREG-Projekts
 1142 GeORG. Teil 1: Ziele und Ergebnisse des Projekts (Zusammenfassung), Freiburg i.Br. /
 1143 Mainz / Strasbourg / Basel.
- 1144 Stein, E., 2001. The geology of the Odenwald Crystalline Complex. *Mineralogy and Petrology*
 1145 72 (1-3), 7–28. <https://doi.org/10.1007/s007100170024>.
- 1146 Stellrecht, R., 1971. Geologisch-tektonische Entwicklung im Raum Albersweiler/Pfalz.
 1147 *Jber_oberrh* 53, 239–262. <https://doi.org/10.1127/jmogv/53/1971/239>.
- 1148 Stober, I., Bucher, K., 2007. Hydraulic properties of the crystalline basement. *Hydrogeol J* 15,
 1149 213–224. <https://doi.org/10.1007/s10040-006-0094-4>.
- 1150 Stollhofen, H., 1998. Facies architecture variations and seismogenic structures in the
 1151 Carboniferous–Permian Saar–Nahe Basin (SW Germany): evidence for extension-related
 1152 transfer fault activity. *Sedimentary Geology* 119 (1-2), 47–83.
 1153 [https://doi.org/10.1016/S0037-0738\(98\)00040-2](https://doi.org/10.1016/S0037-0738(98)00040-2).
- 1154 Suess, F.E., 1926. *Intrusion-und Wandertektonik im variszischen Grundgebirge*. Gebr.
 1155 Bornträger, Berlin, 286 pp.
- 1156 Timmermann, Martin, 2008. Palaeozoic magmatism, in: McCann, T. (Ed.), *The Geology of*
 1157 *Central Europe: Volume 2: Mesozoic and Cenozoic*. Geological Society of London,
 1158 London.

- 1159 Ündül, Ö., 2016. Assessment of mineralogical and petrographic factors affecting petro-
 1160 physical properties, strength and cracking processes of volcanic rocks. *Engineering*
 1161 *Geology* 210, 10–22. <https://doi.org/10.1016/j.enggeo.2016.06.001>.
- 1162 van Zyl, J.J., 2001. The Shuttle Radar Topography Mission (SRTM): a breakthrough in
 1163 remote sensing of topography. *Acta Astronautica* 48 (5-12), 559–565.
 1164 [https://doi.org/10.1016/S0094-5765\(01\)00020-0](https://doi.org/10.1016/S0094-5765(01)00020-0).
- 1165 Vilà, M., Fernández, M., Jiménez-Munt, I., 2010. Radiogenic heat production variability of
 1166 some common lithological groups and its significance to lithospheric thermal modeling.
 1167 *Tectonophysics* 490 (3-4), 152–164. <https://doi.org/10.1016/j.tecto.2010.05.003>.
- 1168 Villemin, T., Alvarez, F., Angelier, J., 1986. The Rhinegraben: Extension, subsidence and
 1169 shoulder uplift. *Tectonophysics* 128 (1-2), 47–59. [https://doi.org/10.1016/0040-1951\(86\)90307-0](https://doi.org/10.1016/0040-1951(86)90307-0).
- 1170
 1171 Villemin, T., Bergerat, F., 1987. L'evolution structurale du fosse rhenan au cours du
 1172 Cenozoïque ; un bilan de la deformation et des effets thermiques de l'extension. *Bulletin*
 1173 *de la Société Géologique de France* III, 245–255.
 1174 <https://doi.org/10.2113/gssqfbull.III.2.245>.
- 1175 Weber, K., 1995a. IV.C.3 The Saar-Nahe Basin, in: Dallmeyer, R.D., Franke, W., Weber, K.
 1176 (Eds.), *Pre-Permian Geology of Central and Eastern Europe*. Springer Berlin Heidelberg,
 1177 Berlin, Heidelberg, pp. 182–185.
- 1178 Weber, K., 1995b. IV.C.4 Structural Relationship Between Saar-Nahe Basin, Odenwald, and
 1179 Spessart Mts., in: Dallmeyer, R.D., Franke, W., Weber, K. (Eds.), *Pre-Permian Geology*
 1180 *of Central and Eastern Europe*. Springer Berlin Heidelberg, Berlin, Heidelberg, pp. 186–
 1181 189.
- 1182 Weinert, S., Bär, K., Sass, I., 2020a. Database of Petrophysical Properties of the Mid-
 1183 German Crystalline High. in review. *Earth Syst. Sci. Data Discuss.*
 1184 <https://doi.org/10.5194/essd-2020-211>.
- 1185 Weinert, S., Bär, K., Sass, I., 2020b. Petrophysical Properties of the Mid-German Crystalline
 1186 High: A Database for Bavarian, Hessian, Rhineland-Palatinate and Thuringian Outcrops.
 1187 Technical University of Darmstadt. TUdataLib. <https://doi.org/10.25534/tudatalib-278>.
- 1188 Weinert, S., Bär, K., Sass, I., 2021, in prep. A Geological 3D-Structural Model of the Hessian
 1189 Mid-German Basement. TUdataLib.
- 1190 Welsch, B., Bär, K., Rühaak, W., Sass, I., 2014. An Outcrop Analogue Study on the
 1191 Suitability of Crystalline Rocks as Heat Storage Media, in: Röhling, H.G., Zulauf, G.
 1192 (Eds.), *GeoFrankfurt 2014 - Dynamik des Systems Erde / Earth Systems Dynamics*,
 1193 Abstract Volume. Schweizerbart Science Publishers, Stuttgart, p. 546.
- 1194 Will, T.M., Lee, S.-H., Schmädicke, E., Frimmel, H.E., Okrusch, M., 2015. Variscan terrane
 1195 boundaries in the Odenwald–Spessart basement, Mid-German Crystalline Zone: New
 1196 evidence from ocean ridge, intraplate and arc-derived metabasaltic rocks. *Lithos* 220-223,
 1197 23–42. <https://doi.org/10.1016/j.lithos.2015.01.018>.
- 1198 Zeh, A., Gerdes, A., 2010. Baltica- and Gondwana-derived sediments in the Mid-German
 1199 Crystalline Rise (Central Europe): Implications for the closure of the Rheic ocean.
 1200 *Gondwana Research* 17 (2-3), 254–263. <https://doi.org/10.1016/j.gr.2009.08.004>.
- 1201 Ziegler, P.A., 1990. Geological atlas of western and central Europe 1990, 2nd ed. Shell
 1202 Internationale Petroleum Maatschappij BV, The Hague, 239 pp.
- 1203 Ziegler, P.A., 1992. European Cenozoic rift system. *Tectonophysics* 208 (1-3), 91–111.
 1204 [https://doi.org/10.1016/0040-1951\(92\)90338-7](https://doi.org/10.1016/0040-1951(92)90338-7).
- 1205 Ziegler, P.A., Dèzes, P., 2005. Evolution of the lithosphere in the area of the Rhine Rift
 1206 System. *International Journal of Earth Sciences* 94 (4), 594–614.
 1207 <https://doi.org/10.1007/s00531-005-0474-3>.